

# Hyperbolic recurrent neural network as the first type of non-Euclidean neural quantum state ansatz

H. L. Dao\*

June 10, 2025

## Abstract

In this work, we introduce the first type of non-Euclidean neural quantum state (NQS) ansatz, in the form of the hyperbolic GRU (a variant of recurrent neural networks (RNNs)), to be used in the Variational Monte Carlo method of approximating the ground state wavefunction for quantum many-body systems. In particular, we examine the performances of NQS ansatzes constructed from both conventional or Euclidean RNN/GRU and from hyperbolic GRU in the prototypical settings of the one- and two-dimensional transverse field Ising models (TFIM) and the one-dimensional Heisenberg  $J_1J_2$  and  $J_1J_2J_3$  systems with varying values of  $(J_1, J_2)$  and  $(J_1, J_2, J_3)$ . By virtue of the fact that, for all of the experiments performed in this work, hyperbolic GRU can yield performances comparable to or better than Euclidean RNNs, which have been extensively studied in these settings in the literature, our work is a proof-of-concept for the viability of hyperbolic GRU as the first type of non-Euclidean NQS ansatz for quantum many-body systems. Furthermore, in settings where the Hamiltonian displays a clear hierarchical interaction structure, such as the 1D Heisenberg  $J_1J_2$  &  $J_1J_2J_3$  systems with the first, second and even third nearest neighbor interactions, our results show that hyperbolic GRU definitively outperforms its Euclidean version in almost all instances. Additionally, in the 2D TFIM setting, 1D hyperbolic GRU NQS also outperform 1D Euclidean GRU NQS, due to the presence of a hierarchical interaction structure comprising the first and  $N^{th}$  nearest neighbor interactions, introduced by the rearrangement of the 1D spin chain to mimic the 2D lattice. The fact that these results are reminiscent of the established ones from natural language processing where hyperbolic GRU almost always outperforms Euclidean RNNs when the training data exhibit a tree-like or hierarchical structure leads us to hypothesize that hyperbolic GRU NQS ansatz would likely outperform Euclidean RNN/GRU NQS ansatz in quantum spin systems that involve different degrees of nearest neighbor interactions. Finally, with this work, we hope to initiate future studies of other types of non-Euclidean neural quantum states beyond hyperbolic GRU.

## Contents

<b>1</b>	<b>Introduction</b>	<b>2</b>
<b>2</b>	<b>Variational Monte Carlo (VMC)</b>	<b>3</b>
<b>3</b>	<b>Hyperbolic RNN and GRU</b>	<b>4</b>
3.1	Poincaré ball model of hyperbolic space	4
3.2	From Euclidean RNN to Hyperbolic RNN	5
3.3	From Euclidean GRU to Hyperbolic GRU	6
3.4	Optimizing hyperbolic parameters	7
<b>4</b>	<b>Euclidean/Hyperbolic RNN-based Neural Quantum State</b>	<b>7</b>
4.1	Real NQS wavefunction	7
4.2	Complex NQS wavefunction	9
<b>5</b>	<b>VMC with hyperbolic RNN-based NQS</b>	<b>10</b>
5.1	1D Transverse Field Ising Model	11
5.1.1	Experiment details	11
5.1.2	Results	12
5.2	2D Transverse Field Ising Model	13
5.2.1	Experiment details	13
5.2.2	Results	15

\*espoirdujour1162@gmail.com

5.3	1D Heisenberg $J_1J_2$ Model . . . . .	17
5.3.1	Experiment details . . . . .	17
5.3.2	Results . . . . .	18
5.4	1D Heisenberg $J_1J_2J_3$ Model . . . . .	20
5.4.1	Experiment details . . . . .	20
5.4.2	Results . . . . .	21
<b>6</b>	<b>Concluding remarks</b>	<b>24</b>
<b>A</b>	<b>Convergence curves</b>	<b>25</b>
A.1	1D TFIM . . . . .	25
A.2	2D TFIM . . . . .	26
A.3	1D Heisenberg $J_1J_2$ model . . . . .	27
A.4	1D Heisenberg $J_1J_2J_3$ model . . . . .	28
<b>References</b>		<b>30</b>

## 1 Introduction

With the advance of deep learning in physics, neural networks have been established as efficient variational trial wavefunctions (variational ansatzes) to estimate the ground states of quantum systems starting with the work of [1] that introduced restricted Boltzmann machines (RBM) as viable candidates for the trial wavefunctions in the spin model settings of 1D Ising model, 1D and 2D Heisenberg models. Since then, in addition to RBM being further employed as variational ansatz in various quantum systems [4], [13], many other types of neural networks have also been constructed and shown to be viable trial/variational wavefunctions in a variety of different problem settings in quantum and condensed matter physics ranging from spin systems [1] - [12], fermion systems [22]-[25], itinerant boson systems [20], [21] to matrix models [14], [40] in the recent literature. Some notable examples of these include ANN-based ansatzes [2], [3], CNN-based ansatzes [6], [7], [8], RNN-based ansatzes [9], [10], [11], [12], transformer-based ansatzes [15], [16] [17], [18], [19] and even generative networks like autoregressive [5] and normalizing-flow-based ansatzes [14], [40]. Collectively, this class of trial wavefunctions based on neural network models are known as neural quantum states (NQS). Very recently, a type of foundation NQS, based on the transformer architecture and introduced in the work [26], is the first type of versatile NQS capable of processing multimodal inputs comprised of spin configurations and Hamiltonian couplings, and generalizing beyond those Hamiltonians encountered during its training phase. Beyond the task of approximating the ground state, extensions of NQS for approximating the excited states are also an active direction of research [27]. A recent review of NQS, including the different neural network architectures used and their many applications in quantum many-body physics can be found in [28] and references therein.

In this work, we present the first type of non-Euclidean NQS based on hyperbolic recurrent neural networks (RNNs). This type of hyperbolic RNNs, whose underlying hyperbolic geometry is that of a Poincaré ball, was introduced in the work of [30] in the context of natural language processing for the tasks of sentence embeddings, textual entailment and noisy-prefix recognition. For these tasks, hyperbolic RNNs have been shown to outperform their Euclidean counterparts, especially in settings when there the training data possess an inherent hierarchical structure [30], [33], [35]. Besides the Poincaré model, another variant of hyperbolic RNNs based on the Lorentz model [31] was proposed and deployed to carry out the NLP task of learning hierarchies in unstructured similarity scores. Besides hyperbolic RNNs, other types of hyperbolic networks, such as hyperbolic CNNs [36], hyperbolic attention networks [34], hyperbolic transformers [32], hyperbolic normalizing flows [33], also have been introduced in quick succession to tackle different NLP-related tasks in deep learning. In [32], the authors demonstrated the superior performances of Lorentz-based hyperbolic networks, including hyperbolic transformers, over their Euclidean versions, in the tasks of machine translation and knowledge graph completion. Regardless of the underlying hyperbolic model, i.e. either Poincaré or Lorentz, hyperbolic neural networks have consistently demonstrated their ability to better learn from and model data with latent hierarchies [30]-[35]. Beyond hyperbolic geometry, the possibility of constructing and deploying other neural networks based on different types of non-Euclidean geometries in deep learning has opened up new and exciting research directions for the relatively new field of non-Euclidean machine learning, whose examples include mixed-curvature variational autoencoders [37], constant curvature graph convolution neural networks [38] among others.

Here, in the context of quantum many-body physics, we will reconfigure the hyperbolic GRU (Gated Recurrent Unit) as defined in [30] to be used as the first type of non-Euclidean NQS ansatz in the prototypical settings of the 1D and 2D transverse field Ising model (TFIM) as well as the 1D Heisenberg  $J_1J_2$  and  $J_1J_2J_3$  models. These models are the most basic testing grounds for a variety of experiments involving neural quantum

states as demonstrated in the earliest works [1], [2] on this topic. With the aim of determining the viability and competitiveness of the hyperbolic GRU as an NQS ansatz, in each of these settings (Ising and Heisenberg models), the performance of the hyperbolic GRU ansatz will be benchmarked firstly against the DMRG (Density Matrix Renormalization Group) results and secondly against that of the conventional or Euclidean RNN/GRU ansatz introduced in the work of [9]. Our obtained results not only demonstrate this feasibility but also potentially open up the possibility of better performances with hyperbolic GRU in quantum settings that exhibit hierarchical structure. Although more work are needed to conclusively confirm this observation in quantum systems beyond those studied in this work, given these first promising results, we hope to highlight the potential of non-Euclidean NQS in quantum many-body physics.

This paper is organized as follows. In section 2, we recall the details of the Variational Monte Carlo (VMC) method to approximate the ground state energy of a quantum system. In section 3, we summarize the mathematical details of the Poincaré model of hyperbolic space in 3.1 and describe the mathematical constructions of hyperbolic RNN (in 3.2) and of hyperbolic GRU (in 3.3) from their respective Euclidean versions. In section 4, we describe the construction of the neural quantum state trial wavefunction using RNNs, with the real case described in 4.1 and complex case described in 4.2. In section 5, we present the main results obtained by using hyperbolic and Euclidean RNNs as variational ansatzes in the settings of 1D TFIM (section 5.1), 2D TFIM (section 5.2), 1D Heisenberg  $J_1 J_2$  model (section 5.3) and 1D Heisenberg  $J_1 J_2 J_3$  model (section 5.4). Section 6 closes the paper with some concluding remarks. In the appendix, we include the convergence curves for the mean energy and variance of all VMC experiments obtained during the training process.

The Python codes used in this work to construct the hyperbolic GRU (using `Tensorflow`)<sup>1</sup> and to run all VMC experiments<sup>2</sup> as well as all the trained neural networks can be found at this Github repository: [https://github.com/lorrespz/nqs\\_hyperbolic\\_rnn](https://github.com/lorrespz/nqs_hyperbolic_rnn).

## 2 Variational Monte Carlo (VMC)

The Variational Monte Carlo (VMC) method, often used to train NQS, involves the process of sampling from a probability distribution represented by the square of the trial wavefunction/the variational ansatz and subsequently using these generated samples to calculate some observables such as the ground state energy. In this section, we recall the derivation of the local energy formula in the Variational Monte Carlo (VMC) method [29].

Given a quantum Hamiltonian  $H$  and the complete basis  $|x\rangle$  satisfying  $\sum_{|x\rangle} |x\rangle\langle x| = 1$ , the trial/variational wavefunction  $|\Psi\rangle$  of this quantum system represented by  $H$  can be written in terms of the basis  $|x\rangle$  as

$$|\Psi\rangle = \sum_{|x\rangle} |x\rangle\langle x|\Psi\rangle = \sum_{|x\rangle} \Psi(x)|x\rangle, \quad (1)$$

where  $\Psi(x) = \langle x|\Psi\rangle$ . The variational energy is the expectation of the Hamiltonian with respect to  $|\Psi\rangle$

$$E = \frac{\langle \Psi | H | \Psi \rangle}{\langle \Psi | \Psi \rangle} \quad (2)$$

and can be shown to assume the following form<sup>3</sup>

$$E = \sum_{|x\rangle} P_{\text{loc}}(x) E_{\text{loc}}(x) \quad (4)$$

where  $P_{\text{loc}}(x)$  is the probability

$$P_{\text{loc}}(x) = \frac{|\langle \Psi | x \rangle|^2}{\sum_{|x\rangle} |\langle \Psi | x \rangle|^2} \quad (5)$$

<sup>1</sup>For the construction of the hyperbolic GRU neural network, we adapted the Tensorflow-v1 (TF1) codes of [30] written for hyperbolic RNNs in the context of natural language processing tasks, which can be found at [https://github.com/dalab/hyperbolic\\_nn](https://github.com/dalab/hyperbolic_nn), to the Tensorflow version 2 (TF2) used in this work

<sup>2</sup>For the VMC experiments as well as the construction of general RNN-based NQS ansatzes, we adapted the Tensorflow v1 (TF1) codes of [9] found at <https://github.com/mhibatallah/RNNWavefunctions/> to Tensorflow v2 (TF2) with the addition of the hyperbolic GRU ansatz.

<sup>3</sup>The derivation of Eq.(4) is as follows

$$\begin{aligned} E &= \frac{\langle \Psi | H | \Psi \rangle}{\langle \Psi | \Psi \rangle} = \frac{\sum_{|x\rangle} \langle \Psi | x \rangle \langle x | H | \Psi \rangle}{\sum_{|x\rangle} \langle \Psi | x \rangle \langle x | \Psi \rangle} = \sum_{|x\rangle} \frac{\langle \Psi | x \rangle}{\sum_{|x\rangle} |\langle \Psi | x \rangle|^2} \sum_{|x'\rangle} \langle x | H | x' \rangle \langle x' | \Psi \rangle \\ &= \sum_{|x\rangle} \frac{|\langle \Psi | x \rangle|^2}{\sum_{|x\rangle} |\langle \Psi | x \rangle|^2} \sum_{|x'\rangle} \langle x | H | x' \rangle \frac{\langle x' | \Psi \rangle}{\langle x | \Psi \rangle} = \sum_{|x\rangle} P_{\text{loc}}(x) E_{\text{loc}}(x) \end{aligned} \quad (3)$$

of obtaining the local energy  $E_{\text{loc}}(x)$ , which is

$$E_{\text{loc}}(x) = \sum_{x'} \langle x | H | x' \rangle \frac{\langle x' | \Psi \rangle}{\langle x | \Psi \rangle}. \quad (6)$$

$E_{\text{loc}}(x)$  is non-zero only for those non-zero Hamiltonian elements  $\langle x | H | x' \rangle \neq 0$ . Using the notation  $\langle x | \Psi \rangle = \Psi(x)$ , we have

$$P_{\text{loc}}(x) = \frac{|\Psi(x)|^2}{\sum_{|x|} |\Psi(x)|^2}, \quad E_{\text{loc}}(x) = \sum_{x'} \langle x | H | x' \rangle \frac{\Psi(x')}{\Psi(x)}. \quad (7)$$

In the variational problem of interest, given a Hamiltonian  $H$  and a trial wavefunction  $\Psi$ , we would like to estimate the ground state energy  $E = \langle \Psi | H | \Psi \rangle$  in Eq.(4) based on the local energy  $E_{\text{loc}}$  given by Eq.(6). When the trial wavefunction is a neural network quantum state  $|\Psi(\vec{\theta})\rangle$  with trainable parameters  $\vec{\theta}$ , at each training iteration  $i$ , the variational energy  $E(\vec{\theta})$  is calculated from the local energy  $E_{\text{loc}}(\vec{\theta})$  of the Monte Carlo samples generated from the NQS. The process of minimizing  $E(\vec{\theta})$  using an optimizer (such as SGD - Stochastic Gradient Descent or Adam - Adaptive Moment Estimation) updates the trainable parameters  $\vec{\theta}$  until convergence is reached.

### 3 Hyperbolic RNN and GRU

#### 3.1 Poincaré ball model of hyperbolic space

In this section, we will summarize and recall the relevant formulas that were originally introduced in [30] to mathematically construct the hyperbolic RNN. The specific hyperbolic space model used in this construction is the Poincaré ball model  $(\mathbb{D}^N, g^{\mathbb{D}})$  defined by the manifold  $\mathbb{D}^N$

$$\mathbb{D}_c^N = \{x \in \mathbb{R}^N : c\|x\| < 1\} \quad (8)$$

where the parameter  $c$  is the Poincaré ball's radius. When  $c = 0$ ,  $\mathbb{D}_c^N = \mathbb{R}^N$ , while when  $c > 0$ ,  $\mathbb{D}_c^N$  is the open ball of radius  $1/\sqrt{c}$ . In all the computations used in this work, we set  $c = 1$ . The space  $\mathbb{D}_c^N$  in Eq.(8) is equipped with the metric

$$g_x^{\mathbb{D}} = \lambda_x^2 g^E, \quad \lambda_x = \frac{2}{1 - \|x\|^2} \quad (9)$$

where  $g^E = \mathbf{1}_N$  is the identity matrix representing the Euclidean metric. On a curved space, all arithmetic operations involving scalars and matrices (such as addition and multiplication) have to be redefined to take into account the geometry of the space. We will not repeat the derivation here (as the full details can be found in [30]) but simply quote the formulas that were actually used to define the hyperbolic RNN. In this section, only the most basic geometrical operations (such as addition, scalar multiplication, maps between hyperbolic space and its tangent space and parallel transport) will be defined since they are used to construct other operations such as pointwise nonlinearity and matrix multiplication, which will be defined in later sections in the order that they appear. The derivations and proofs for all formulas can be found in [30].

- The most basic operation in terms of which all other operations are defined is the Möbius addition  $\oplus_c$  between scalars  $x, y \in \mathbb{D}_c^N$ .

$$x \oplus_c y \equiv \frac{(1 + 2c\langle x, y \rangle + c\|y\|^2)x + (1 - c\|x\|^2)y}{1 + 2c\langle x, y \rangle + c^2\|x\|^2\|y\|^2}. \quad (10)$$

This operation is neither commutative nor associative but satisfies the following  $(-x) \oplus_c x = x \oplus_c (-x) = \mathbf{0}$ . When  $c = 0$ , the usual Euclidean addition operation is recovered  $\lim_{c \rightarrow 0} x \oplus_c y = x + y$ .

- For any point  $x \in \mathbb{D}_c^N$ , any vector  $v \neq \mathbf{0}$  and any point  $y \neq x$ , the exponential and logarithmic maps  $\exp_x^c : T_x \mathbb{D}_c^N \rightarrow \mathbb{D}_c^N$  and  $\log_x^c : \mathbb{D}_c^N \rightarrow T_x \mathbb{D}_c^N$  between the hyperbolic space and its Euclidean tangent space are defined as

$$\exp_x^c(v) = x \oplus_c \left[ \tanh\left(\sqrt{c} \frac{\lambda_x^c \|v\|}{2}\right) \frac{v}{\sqrt{c} \|v\|} \right] \quad (11)$$

$$\log_x^c(y) = \frac{2}{\sqrt{c} \lambda_x^c} \tanh^{-1} \left( \sqrt{c} \| -x \oplus_c y \| \right) \frac{-x \oplus_c y}{\| -x \oplus_c y \|} \quad (12)$$

where  $\lambda_x^c = 2/(1-c|x|^2)$ . Note that  $\log_x^c$  and  $\exp_x^c$  as defined in the above equations satisfies  $\log_x^c(\exp_x^c(v)) = v$ . When  $x = \mathbf{0}$ , the above maps take more compact forms

$$\exp_{\mathbf{0}}^c(v) = \tanh(\sqrt{c}|v|) \frac{v}{\sqrt{c}|v|} \quad (T_{\mathbf{0}_M} \mathbb{D}_c^M \rightarrow \mathbb{D}_c^M) \quad (13)$$

$$\log_{\mathbf{0}}^c(y) = \tanh^{-1}(\sqrt{c}|y|) \frac{y}{\sqrt{c}|y|} \quad (\mathbb{D}_c^N \rightarrow T_{\mathbf{0}_N} \mathbb{D}_c^N) . \quad (14)$$

Note that when  $c = 0$ , we recover the Euclidean geometry limit  $\lim_{c \rightarrow 0} \exp_x^c(v) = x + v$  and  $\lim_{c \rightarrow 0} \log_x^c(y) = y - x$ .

- The parallel transport  $P_{\mathbf{0} \rightarrow x}^c(v)$  of a vector  $v \in T_{\mathbf{0}} \mathbb{D}_c^N$  to another tangent space  $T_x \mathbb{D}_c^N$  can be defined in terms of the exponential and logarithmic maps of Eq.(13), Eq.(14) as

$$P_{\mathbf{0} \rightarrow x}^c(v) = \log_x^c[x \oplus_c \exp_{\mathbf{0}}^c(v)] \quad (15)$$

In terms of parallel transport, the Möbius addition for  $x \in \mathbb{D}_c^N$  with  $b \in \mathbb{D}_c^N$  can be written as

$$x \oplus_c b = \exp_x^c \left[ P_{\mathbf{0} \rightarrow x}^c \left( \log_{\mathbf{0}}^c(b) \right) \right] \quad (16)$$

- The Möbius scalar multiplication of  $x \in \mathbb{D}_c^N \setminus \{\mathbf{0}\}$  by  $r \in \mathbb{R}$ , denoted by  $\otimes_c$ , is defined as

$$r \otimes_c x = \frac{1}{\sqrt{c}} \tanh(r \tanh^{-1}(\sqrt{c}|x|)) \frac{x}{\|x\|} \quad (17)$$

and  $r \otimes_c \mathbf{0} = \mathbf{0}$ . When  $c = 0$ , the Euclidean scalar multiplication is recovered  $\lim_{c \rightarrow 0} r \otimes_c x = rx$ . Interestingly,  $r \otimes_c x$  can also be expressed in terms of the  $\exp_{\mathbf{0}}^c$  and  $\log_{\mathbf{0}}^c$  maps defined in Eqs.(13, 14) as

$$r \otimes_c x = \exp_{\mathbf{0}}^c(r \log_{\mathbf{0}}^c(x)), \quad \forall r \in \mathbb{R}, x \in \mathbb{D}_c^N. \quad (18)$$

### 3.2 From Euclidean RNN to Hyperbolic RNN

Given an input vector  $\vec{x}_i \in \mathbb{R}^{d_x}$  at step  $i^{\text{th}}$  of size  $d_x$ , the defining equation for the Euclidean or conventional version of RNN is one that relates the hidden state vector  $h_i \in \mathbb{R}^{d_h}$  of size  $d_h$  to the input  $x_i$  and the same hidden state vector at the previous time step  $(i-1)^{\text{th}}$

$$\text{RNN} : \quad \vec{h}_i = f(W_h \vec{h}_{i-1} + U_h \vec{x}_i + \vec{b}_h), \quad (19)$$

where  $W_h$  is a  $d_h \times d_h$  weight matrix,  $U_h$  is a  $d_h \times d_x$  weight matrix, and  $b_h \in \mathbb{R}^{d_h}$  is a vector of size  $d_h$  known as the bias. Using Eq.(19), we can convert the Euclidean RNN to the hyperbolic RNN using

$$\text{Hyperbolic RNN} : \quad \vec{h}_i = f^{\otimes_c} \left[ (W_h \otimes_c \vec{h}_{i-1}) \oplus_c (U_h \otimes_c \vec{x}_i) \oplus_c \vec{b}_h \right] \quad (20)$$

where  $W_h, U_h$  have the same meanings as in the Euclidean RNN case, but the hidden state vector  $h_i \in \mathbb{D}_c^{d_h}$ , input vector  $\vec{x}_i \in \mathbb{D}_c^{d_x}$ , and bias vector  $b_h \in \mathbb{D}_c^{d_h}$  are all parts of the hyperbolic space. The operation  $\oplus_c$  is defined in Eq.(10), while the matrix multiplication  $\otimes_c$  and pointwise nonlinearity  $f^{\otimes_c}$  operations are defined in hyperbolic space as follows.

1.  $f^{\otimes_c} : \mathbb{D}_c^N \rightarrow \mathbb{D}_c^M$  is the Möbius-version of the pointwise Euclidean nonlinear activation function  $f : \mathbb{R}^N \rightarrow \mathbb{R}^M$

$$f^{\otimes_c}(x) \equiv \exp_{\mathbf{0}}^c[f\{\log_{\mathbf{0}}^c(x)\}]. \quad (21)$$

where  $\exp_{\mathbf{0}}^c$  and  $\log_{\mathbf{0}}^c$  are defined in Eq.(13) and Eq.(14). When  $c = 0$ , we recover the Euclidean limit  $\lim_{c \rightarrow 0} f^{\otimes_c}(x) = f(x)$ .

2. The matrix-vector multiplication  $\otimes_c$  acting on the vector  $x \in \mathbb{D}^N$  is the Möbius-version of the Euclidean matrix multiplication involving  $W : \mathbb{R}^M \rightarrow \mathbb{R}^N$  that acts on  $x \in \mathbb{R}^N$  with  $Wx \neq \mathbf{0}$ , and is defined as

$$W \otimes_c (x) = \frac{1}{\sqrt{c}} \tanh \left( \frac{\|Wx\|}{\|x\|} \tanh^{-1}(\sqrt{c}|x|) \right) \frac{Wx}{\|Wx\|}. \quad (22)$$

Note that  $W \otimes_c x = \mathbf{0}$  if  $Wx = \mathbf{0}$ .

Finally, we note that when the input  $\vec{x}_i$  in Eq.(20) is in Euclidean space, we can still use the Eq.(20) by making use of  $\vec{z}_i = \exp_0^c(\vec{x}_i)$ <sup>4</sup> so that Eq.(19) becomes

$$\vec{h}_i = f^{\otimes_c} \left[ (W_h \otimes_c \vec{h}_{i-1}) \oplus_c (U_h \otimes_c \vec{z}_i) \oplus_c \vec{b}_h \right]. \quad (24)$$

In this work, we will not make use of the RNN variant of hyperbolic RNNs, but its construction serves as an intermediate step in understanding the construction of the hyperbolic GRU variant, which is discussed in the next section.

### 3.3 From Euclidean GRU to Hyperbolic GRU

GRU is a more sophisticated version of RNN with additional structures comprising the reset gate  $r_i$  and the update gate  $z_i$ . The defining equations of the conventional or Euclidean GRU are

$$\text{GRU : } \vec{r}_i = \sigma \left( W_r \vec{h}_{i-1} + U_r \vec{x}_i + \vec{b}_r \right) \quad (25)$$

$$\vec{z}_i = \sigma \left( W_z \vec{h}_{i-1} + U_z \vec{x}_i + \vec{b}_z \right) \quad (26)$$

$$\vec{h}_i = f \left[ W_h (\vec{r}_i \odot \vec{h}_{i-1}) + U_h \vec{x}_i + \vec{b}_h \right] \quad (27)$$

$$\vec{h}_i = (1 - z_i) \odot \vec{h}_{i-1} + z_i \odot \vec{h}_i \quad (28)$$

In the above equations,  $f$  is a nonlinear activation function,  $\sigma$  is the sigmoid activation,  $\vec{x}_i$  is the input vector of length  $d_x$ ,  $W_h, W_z, W_r$  are the  $d_h \times d_h$  weight matrices,  $U_h, U_z, U_r$  are the  $d_h \times d_x$  weight matrices,  $\vec{b}_h, \vec{b}_z, \vec{b}_r \in \mathbb{R}^{d_h}$  are the bias vectors, and  $\odot$  is the pointwise multiplication operation.

The equations Eqs.(25)-(28) above can be converted to the defining equation of the hyperbolic GRU using the hyperbolic operations  $\oplus_c, \otimes_c, f^{\otimes_c}$  defined in Eqs.(10), (22), (21) as follows.

- First, the equations Eq.(25), Eq.(26) for the reset gate  $\vec{r}_i$  and update gate  $\vec{z}_i$  are updated to

$$\begin{aligned} \vec{r}_i &= \sigma \log_0^c \left[ (W_r \otimes_c \vec{h}_{i-1}) \oplus_c (U_r \otimes_c \vec{x}_i) \oplus_c \vec{b}_r \right] \\ \vec{z}_i &= \sigma \log_0^c \left[ (W_z \otimes_c \vec{h}_{i-1}) \oplus_c (U_z \otimes_c \vec{x}_i) \oplus_c \vec{b}_z \right] \end{aligned}$$

- The term  $\vec{r}_i \odot \vec{h}_{i-1}$  containing the pointwise multiplication operation  $\odot$  is adapted to

$$\vec{r}_i \odot \vec{h}_{i-1} \rightarrow \text{diag}(r_i) \otimes_c \vec{h}_{i-1}.$$

where  $\text{diag}(r_i)$  denotes the diagonal matrix of size  $d_h \times d_h$  with the diagonal entries being the entries of the vector  $r_i$  (of length  $d_h$ ).

- The intermediate hidden state  $\vec{h}_i$  in Eq.(27) is converted to

$$\vec{h}_i = f^{\otimes_c} \left[ (W \text{diag}(r_t)) \otimes_c \vec{h}_{i-1} \oplus (U \otimes_c \vec{x}_i) \oplus_c \vec{b}_h \right]$$

- The final GRU update equation, Eq.(28), is converted to

$$\vec{h}_i = \vec{h}_{i-1} \oplus_c \text{diag}(z_i) \otimes_c \left( -\vec{h}_{i-1} \oplus \vec{h}_i \right) \quad (29)$$

Putting together all the update equations, we have the following defining equations for the hyperbolic GRU

$$\vec{r}_i = \sigma \log_0^c \left[ (W_r \otimes_c \vec{h}_{i-1}) \oplus_c (U_r \otimes_c \vec{x}_i) \oplus_c \vec{b}_r \right], \quad (30)$$

$$\vec{z}_i = \sigma \log_0^c \left[ (W_z \otimes_c \vec{h}_{i-1}) \oplus_c (U_z \otimes_c \vec{x}_i) \oplus_c \vec{b}_z \right], \quad (31)$$

$$\vec{h}_i = f^{\otimes_c} \left[ (W \text{diag}(r_t)) \otimes_c \vec{h}_{i-1} \oplus (U \otimes_c \vec{x}_i) \oplus_c \vec{b}_h \right], \quad (32)$$

$$\vec{h}_i = \vec{h}_{i-1} \oplus_c \text{diag}(z_i) \otimes_c \left( -\vec{h}_{i-1} \oplus \vec{h}_i \right). \quad (33)$$

<sup>4</sup>This is because using Eq.(16) we have

$$\exp_{W \otimes_c \vec{h}_i} \left[ P_{\mathbf{0} \rightarrow W \otimes_c \vec{h}_i}^c (U \vec{x}_i) \right] = (W \otimes_c \vec{h}_i) \oplus_c \exp_0^c (U \vec{x}_i) = (W \otimes_c \vec{h}_i) \oplus_c (U \otimes_c \vec{z}_i) \quad (23)$$

### 3.4 Optimizing hyperbolic parameters

Hyperbolic RNN/GRU can be used in conjunction with Euclidean Dense layers in a ‘plug-and-play’ manner as noted by the authors of [30]. However, in going from hyperbolic to Euclidean layers, one must apply the exponential and logarithmic maps in Eq.(13) and Eq.(14) accordingly. Furthermore, hyperbolic parameters must be optimized separately from their Euclidean counterparts using ‘hyperbolic’ optimizer, which is chosen in this work to be RSGD - Riemannian Stochastic Gradient Descent [41], [42], [43]. To define RSGD, one starts from SGD, which is an update rule for a variable  $x$  at time step  $t$

$$x_{t+1} \leftarrow x_t - \alpha g_t \quad (34)$$

where  $g_t$  is the gradient of the objective/cost function  $f_t$  and  $\alpha > 0$  is the learning rate. In a Riemannian manifold  $\mathcal{M}$  equipped with metric  $g$ ,  $(\mathcal{M}, g)$ , for smooth  $f : \mathcal{M} \rightarrow \mathbb{R}$ , the Riemannian SGD is defined by the following update [41]

$$x_{t+1} \leftarrow \exp_{x_t}(-\alpha g_t) \quad (35)$$

where  $\exp_{x_t} : T_{x_t} \mathcal{M} \rightarrow \mathcal{M}$  is the exponential map defined in Eq.(11), and  $g_t \in T_{x_t} \mathcal{M}$  denotes the Riemannian gradient of  $f_t$  at  $x_t$ . When  $(\mathcal{M}, g) = (\mathbb{R}^n, \mathbf{I}_n)$ , i.e. the  $n$ -dimensional Euclidean space, RSGD in Eq.(35) reduces to SGD in Eq.(34) since  $\exp_x(v) = x + v$  in Euclidean space.

As a final remark in this section, we note that due to the many more mathematical operations involved in defining hyperbolic RNNs compared to their Euclidean counterparts, a drawback of these networks is that they are much more computationally intensive and take much longer to train than Euclidean RNNs. In this work, we only use the GRU variant of hyperbolic RNNs, and not the RNN variant (which tend to underperform GRU)<sup>5</sup>.

## 4 Euclidean/Hyperbolic RNN-based Neural Quantum State

In this section, we describe in detail the RNN-based neural quantum state (NQS). In particular, the architecture of this type of NQS consists of a RNN/GRU unit, which can be either Euclidean or hyperbolic, and one or two dense layer(s), depending on whether the NQS wavefunction is real or complex. The way the RNN-based NQS is defined and constructed here is almost the same as done in [9], with the important exception being the use of hyperbolic GRU. For Euclidean RNN-based NQS (both the GRU and RNN variants), the construction is the same as that of [9] and Euclidean RNN-based NQS is included in this work to provide a performance benchmark for hyperbolic GRU-based NQS.

### 4.1 Real NQS wavefunction

For a discrete  $N$ -dimensional Hamiltonian systems in which the basis states  $|\vec{\sigma}\rangle = (\sigma_1, \dots, \sigma_N)$  with each component  $\sigma_n$  ( $1 \leq n \leq N$ ) assuming the discrete values  $0, 1, \dots, (d_v - 1)$ <sup>6</sup>, the RNN-based neural quantum state is defined as

$$|\Psi\rangle = \sum_{\vec{\sigma}} \sqrt{P(\vec{\sigma})} |\vec{\sigma}\rangle \quad (36)$$

where  $P(\sigma)$  is the output generated by the RNN-based neural network<sup>7</sup>.  $P(\sigma)$  is the probability of a particular configuration  $|\vec{\sigma}\rangle$ , and it is the product of the conditional probabilities  $P(\sigma_n | \sigma_1 \dots s_{n-1})$ .

$$P(\vec{\sigma}) = P(\sigma_1)P(\sigma_2|\sigma_1) \dots P(\sigma_N|\sigma_1, \sigma_2, \dots, \sigma_{N-1}) \quad (39)$$

<sup>5</sup>Throughout this work, however, sometimes we might use the term hyperbolic RNN interchangeably with hyperbolic GRU. This is the case, for example, in the term ‘RNN-based’ where the RNN here can refer to either RNN/GRU (for Euclidean networks) or just GRU (for hyperbolic networks).

<sup>6</sup>For example, a 2-level system has  $d_v = 2$  with two possible values : 0, 1. A 3-level system has  $d_v = 3$  with three possible values 0, 1, 2, and so on

<sup>7</sup>Applying the RNN quantum state Eq.(36) to the variational energy Eq.(6), we have

$$E = \sum_{|\vec{\sigma}\rangle} \left( \frac{P(\vec{\sigma})}{\sum_{|\vec{\sigma}'\rangle} P(\vec{\sigma}')} \right) E_{\text{loc}}(\vec{\sigma}) \quad (37)$$

where the local energy of a generated sample  $\vec{\sigma}$  is

$$E_{\text{loc}}(\vec{\sigma}) = \sum_{|\vec{\sigma}'\rangle} \langle \vec{\sigma} | H | \vec{\sigma}' \rangle \frac{\sqrt{P(\vec{\sigma}')}}{\sqrt{P(\vec{\sigma})}}. \quad (38)$$

The RNN-based neural network representing the NQS in this case consists of a RNN/GRU layer (either Euclidean or hyperbolic), and a dense layer with  $d_v - 1$  units with a Softmax activation function. The process of calculating  $P(\vec{\sigma})$  using this RNN-based NQS is depicted in Fig.1 and described step-by-step below.

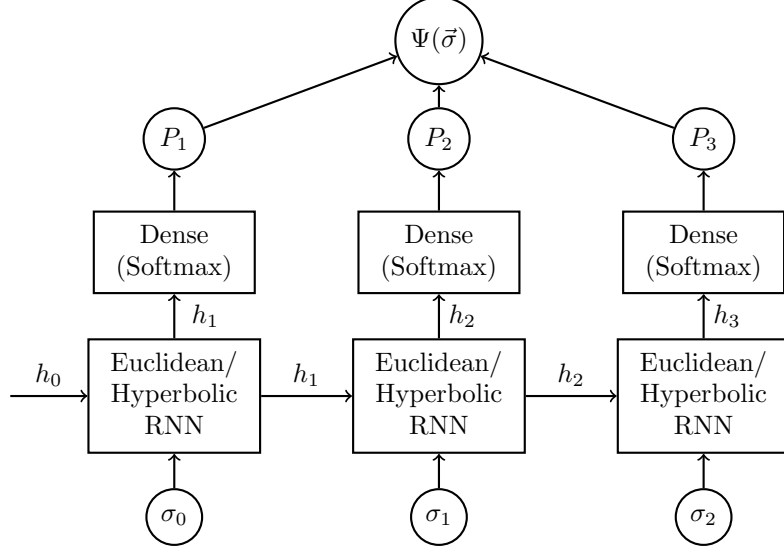


Figure 1: Schematic of the process of calculating the RNN wavefunction  $\Psi(\vec{\sigma}) = \sqrt{P(\vec{\sigma})}|\vec{\sigma}\rangle$  from the probability  $P(\vec{\sigma})$  of the sample  $\vec{\sigma}$ . Here  $P(\vec{\sigma}) = P(\sigma_1)P(\sigma_2|\sigma_1)\dots P(\sigma_N|\sigma_{N-1})$ . For a compact representation,  $N = 4$  in the schematic. The RNN in the diagram can be either Euclidean RNN/GRU or Hyperbolic GRU. Figure adapted from [9].

- At time step  $i$ , given an input  $\vec{\sigma}_{i-1}$  (of dimension  $d_v$ ) and a previous hidden state  $\vec{h}_{i-1}$  of dimension  $d_h$ , the Euclidean/hyperbolic RNN maps it to a new hidden state  $\vec{h}_i$

$$\vec{h}_i = \text{RNN}(\vec{h}_{i-1}, \vec{\sigma}_{i-1}) \quad (40)$$

where the function  $\text{RNN}(\dots)$  is computed using Eq.(19), Eqs.(25)-(28) for Euclidean RNN/GRU and Eqs.(20), Eqs.(30)-(33) for hyperbolic RNN/GRU. The input  $\vec{x}_i$  in those equations are now replaced by  $\vec{\sigma}_i$ , a one-hot encoded vector of length  $d_v$ . When  $i = 1$ , the hidden and initial states  $\vec{h}_0$  and  $\vec{\sigma}_0$  are both set to zero.

If a hyperbolic RNN is used, we need to apply the logarithmic map Eq.(14) on the RNN hidden state  $\vec{h}_i$  before feeding it into the next layer, which is a normal (Euclidean) dense layer.

- The state  $\vec{h}_i$  serves as an argument for the dense layer with a **Softmax** activation function to obtain the output  $y_i$

$$\vec{y}_i = \text{Softmax} \left( U \vec{h}_i + \vec{c} \right), \quad \begin{cases} U \in \mathbb{R}^{d_v \times d_h} : \text{weight matrix} \\ \vec{c} \in \mathbb{R}^{d_h} : \text{bias vector} \end{cases} \quad (41)$$

and the **Softmax** function<sup>8</sup> is

$$\text{Softmax}(v_k) = \frac{\exp(v_k)}{\sum_i \exp(v_i)} \quad (42)$$

$\vec{y}_i$  is a vector of length  $d_v$  whose components sum up to 1. The probability  $P(\sigma_i|\sigma_1\dots s_{i-1})$  is given by

$$P(\sigma_i|\sigma_1\dots s_{i-1}) = \vec{y}_i \cdot \vec{\sigma}_i. \quad (43)$$

Note that  $\vec{\sigma}_i$  is the one-hot encoded vector of length  $d_v$ , not to be confused with  $\vec{\sigma} = (\sigma_1, \dots, \sigma_N)$ , which is a vector of length  $N$ .

- The total probability  $P(\vec{\sigma})$  appearing in Eq.(40) is then

$$P(\vec{\sigma}) = \prod_{n=1}^N \vec{y}_i \cdot \vec{\sigma}_i. \quad (44)$$

<sup>8</sup>which converts a vector of length  $K$  into a probability distribution of  $K$  possible outcomes

The process of generating the samples  $\vec{\sigma}$  is similar to the process of calculating  $P(\vec{\sigma})$  above up to Eq.(41) when the output  $\vec{y}_i$  at time step  $i$  is obtained, after which  $\sigma_i$  is sampled from  $\vec{y}_i$ , and then one-hot encoded and used as input, together with the hidden state  $\vec{h}_{i-1}$ , to repeat the process. Schematically, the generation of samples is shown in Fig.2.

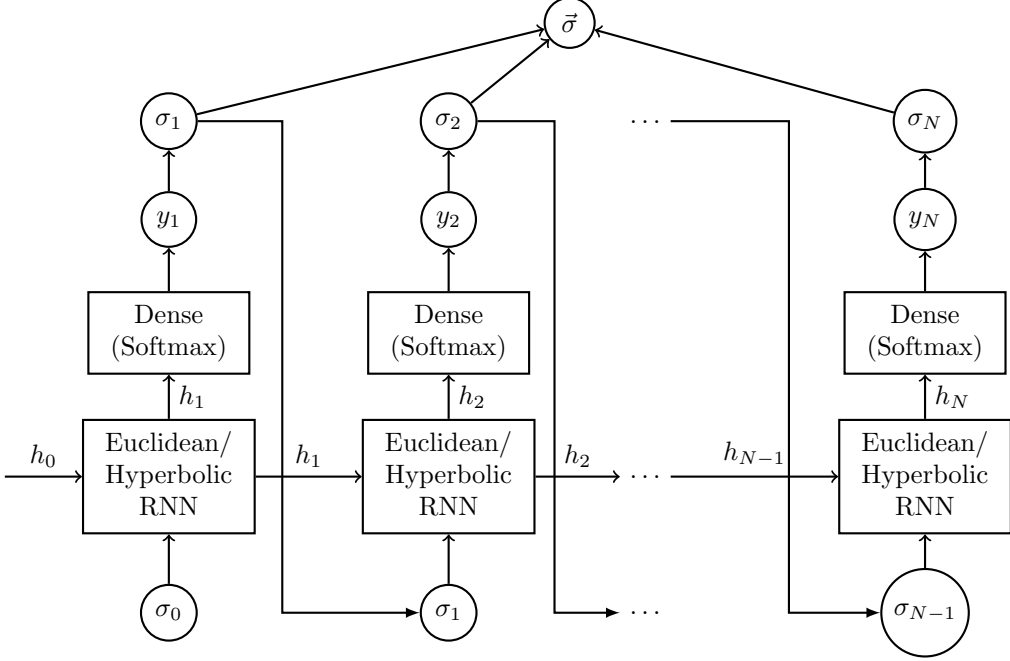


Figure 2: The process of generating the length- $N$  samples  $\vec{\sigma} = (\sigma_1, \dots, \sigma_N)$  using an RNN-based neural network. Each entry  $\sigma_i$  of  $\vec{\sigma}$  is sampled from the output  $y_i$  (generated by the RNN-Dense network using as input the previous entry  $\sigma_{i-1}$  and the previous RNN hidden state  $h_{i-1}$ ) and then one-hot encoded to be used as input, together with the previous hidden state  $h_{i-1}$ , for the generation of the next entry  $\sigma_{i+1}$ . For  $i = 0$ , the input  $\vec{\sigma}_0$  and first hidden state  $h_0$  are initialized to zero. Figure adapted from [9].

## 4.2 Complex NQS wavefunction

The complex RNN-based NQS wavefunction has a phase factor  $\phi(\vec{\sigma})$  in addition to a real amplitude  $P(\vec{\sigma})$ , and is defined as

$$\Psi(\vec{\sigma}) = \sum_{\vec{\sigma}} \exp(i\phi(\vec{\sigma})) \sqrt{P(\vec{\sigma})} |\vec{\sigma}\rangle \quad (45)$$

The architecture of the RNN-based neural network representing the complex NQS differs from that of the RNN-based NQS by an additional Dense layer, with the Softsign function, modeling the phase. The schematic of the complex RNN-based NQS is shown in Fig.3. In Eq.(45), the amplitude  $P(\vec{\sigma})$  is generated using a Softmax layer in the same way as in the case of the real NQS wavefunction, i.e.

$$P(\vec{\sigma}) = \prod_{i=1}^N P(\vec{\sigma}_i), \quad P(\vec{\sigma}_i) = y_i^{(1)} \cdot \vec{\sigma}_i, \quad y_i^{(1)} = \text{Softmax}(U h_i + c) \quad (46)$$

while the phase  $\phi(\vec{\sigma})$  is generated using a Softsign layer. The Softsign function is defined as

$$\text{Softsign}(x) = \frac{x}{1 + |x|} \in (-1, 1). \quad (47)$$

The total phase factor  $\phi(\vec{\sigma})$  of Eq.(45) is the sum of the phase factors  $\phi_i$  resulting from each entry  $\sigma_i$  of  $\vec{\sigma}$

$$\phi(\vec{\sigma}) = \sum_{i=1}^N \phi_i, \quad \phi_i = y_i^{(2)} \cdot \vec{\sigma}_i, \quad (48)$$

where the output  $\vec{y}_i^{(2)}$  is obtained from the Softsign layer

$$\vec{y}_i^{(2)} = \pi \text{Softsign} \left( U^{(2)} \vec{h}_i + c^{(2)} \right) \quad (49)$$

In Eqs.(46), (48), we note that  $\vec{\sigma}_i$  is the one-hot encoded vector with dimension  $d_v$ , and it is the  $i^{th}$  entry of the sample  $\vec{\sigma} = (\sigma_1, \dots, \sigma_N)$ .

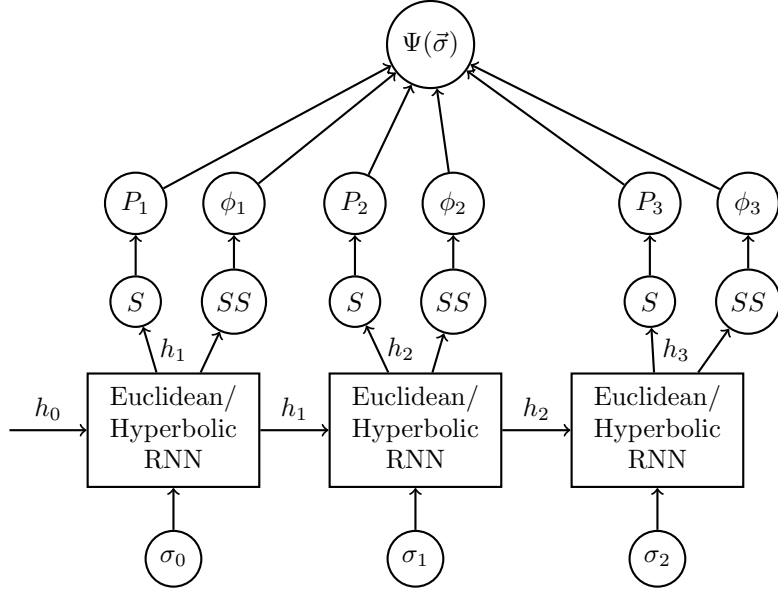


Figure 3: Schematic of the calculation of the RNN wavefunction  $\Psi(\vec{\sigma}) = \sum_{\vec{\sigma}} \exp(i\phi(\vec{\sigma})) \sqrt{P(\vec{\sigma})} |\vec{\sigma}\rangle$  where the amplitude  $P(\vec{\sigma}) = P(\sigma_1)P(\sigma_2|\sigma_1) \dots P(s_N|\sigma_{N-1})$  and the phase  $\phi(\vec{\sigma}) = \sum_{i=1}^N \phi(\vec{\sigma}_i)$ . For ease of illustration,  $N$  is chosen to be 3. (S) and (SS), correspondingly, denote the dense layer with the Softmax and Softsign activation function. Figure adapted from [9].

## 5 VMC with hyperbolic RNN-based NQS

In this section, we report the results of running various VMC experiments for several quantum many-body systems using the GRU variant of hyperbolic RNNs as well as the Euclidean RNN/GRU as ansatzes for the trial ground state wavefunction. In particular, we choose the following four prototypical systems as settings for our VMC experiments:

- One-dimensional Transverse Field Ising model (1D TFIM) - Section 5.1
- Two-dimensional Transverse Field Ising model (2D TFIM) - Section 5.2
- One-dimensional Heisenberg  $J_1J_2$  model (1D  $J_1J_2$ ) - Section 5.3
- One-dimensional Heisenberg  $J_1J_2J_3$  model (1D  $J_1J_2J_3$ ) - Section 5.4

These systems are the most basic testing grounds for different types of NQS ansatzes, and they have been used routinely in the literature on NQS. As benchmark against which to evaluate the performances of all NQS ansatzes, we will use DMRG (Density Matrix Renormalization Group). With 1D systems, DMRG results are considered to be exact, while in 2D systems, this is no longer the case, but this is still a reliable benchmark to use since DMRG provides state-of-the-art computational results for various condensed matter systems.

As the performances of Euclidean RNN-based NQS have been established in the work [9] for the 1D TFIM, 2D TFIM and 1D  $J_1J_2$  systems, we do not aim to replicate their results but instead aiming to establish the performances of hyperbolic GRU-based NQS using the performances of Euclidean RNN/GRU-based NQS as benchmarks in settings of smaller scales, due to the fact that hyperbolic networks are more computationally intensive and take much longer to train than their Euclidean counterparts. Specifically, for the 1D TFIM, the work [9] explored settings up to  $N = 1000$  spins, while we restrict the number of spins in our settings up to  $N = 100$ . For the 2D TFIM, [9] studied a square lattice of size  $(N_x, N_y) = (12, 12)$  while we restrict the lattice size to  $(N_x, N_y) = (9, 9)$ . For the  $J_1J_2$  systems, [9] used a setting involving  $N = 100$  spins while we restrict the number of spins in our setting to  $N = 50$ . The 1D  $J_1J_2J_3$  model was not studied in [9].

## 5.1 1D Transverse Field Ising Model

The Hamiltonian of the one-dimensional transverse field Ising model (1D TFIM) with open boundary condition is

$$H_{1\text{DTFIM}} = -J \sum_{i=1}^{N-1} \sigma_i^z \sigma_{i+1}^z - B \sum_{i=1}^N \sigma_i^x \quad (50)$$

where  $\sigma_x, \sigma_y, \sigma_z$  are the Pauli matrices. The first sum in the Hamiltonian runs over pairs of nearest neighbors, while the second sum runs over all sites in the 1D spin chain. This system is known to exhibit a phase transition at the critical value of  $B = 1$  (with  $J = 1$ ) from a disordered (paramagnetic) to an ordered (ferromagnetic) state.

### 5.1.1 Experiment details

For the 1D TFIM system, we choose four settings with the number of spins  $N$  being 20, 40, 80 and 100. Three different RNN-based real NQS, namely Euclidean RNN, Euclidean GRU and hyperbolic GRU, are used as ansatzes in the VMC experiments for 1D TFIM at each  $N$  (see Table 1). The architecture of these ansatzes is the same as that of the real NQS wavefunction described in Section 4.1, which consists of an RNN (either Euclidean or hyperbolic) with the hidden dimension  $d_h = 50$  and a Dense layer with 2 units (representing the 0 or 1 entry of the spin  $\sigma_i$  at site  $i$ ) with the Softmax activation function. The wavefunction is given by Eq.(36) in which the state  $|\vec{\sigma}\rangle$  is a vector of length  $N$  with each entry assuming a value of either 0 or 1 (spin up or down). The number of spin configuration samples that are generated is kept fixed at 50 for all three ansatzes. This choice is made based on the observation that increasing the number of samples generated does not really improve the results while significantly increasing the training time. The number of parameters of the Euclidean

Ansatz	Name	Parameters
Euclidean RNN	eRNN-50-s50	2752
Euclidean GRU	eGRU-50-s50	8052
Hyperbolic GRU	hGRU-50-s50	8052

Table 1: The variants of NQS ansatzes used for the VMC experiments involving the 1D TFIM Hamiltonian with various system sizes  $N = 20, 40, 80, 100$  for  $J = 1$  and  $B = 1$ .

RNN ansatz is 2752, while the number of parameters of the Euclidean and hyperbolic GRU-based ansatz is 8052. For Euclidean ansatzes, we use `Adam` optimizer with an exponential decay learning rate while for the hyperbolic ansatz, we use RSGD (Riemannian SGD) with the fixed learning rate of  $\alpha = 10^{-2}$  for hyperbolic parameters and the same `Adam` with exponentially decaying learning rate for Euclidean parameters. In the hyperbolic GRU ansatz, only the biases ( $b_h, b_r, b_z$ ) are hyperbolic, while the weight matrices are Euclidean. This configuration is the same as the one used in [30], and is kept unchanged throughout this work.

At each iteration of the training process, a neural network ansatz generates 50 samples (spin configurations) whose mean energy is used to approximate the true ground state energy of the 1D TFIM. Convergence is reached when there is no noticeable change in the mean energy and the energy variance of all the samples is smaller than a certain tolerance threshold. This specific values of the tolerance threshold vary for different VMC experiments, and can range from as low as 0.05 to <sup>9</sup>. For all three types of ansatzes at all  $N$ , convergence is reached very quickly at around 100 epochs with the total number of training steps set at 120 epochs. Even with this very small number of epochs, for the hyperbolic GRU to complete the training loop, it takes around 1.5 hours for  $N = 20$  and up to 10 hours for  $N = 100$  on an average laptop<sup>10</sup> with no GPU. On the other hand, Euclidean RNN and GRU take around 0.1 hours for  $N = 20$  and around 1.5 hours for  $N = 100$  on the same hardware. During the training process, only the best models are saved, i.e. the training loop might continue until the specified number of iterations is reached but unless a better result is obtained, the final model is the last saved model, e.g. if the best model is the one at epoch 65, training still carries on until epoch 120 but no new model is saved after epoch 65 unless there is a better model at the  $i^{th}$  epoch where  $65 < i < 120$ . Unless otherwise stated, these training details (include the type of optimizers, the hardware resource, the number of generated samples used in training, the selected saving of best model) remain the same throughout this work in all VMC experiments.

<sup>9</sup>In other settings such as 2D TFIM, 1D  $J_1 J_2$  models, the variance tolerance can be much higher

<sup>10</sup>a average laptop at the time of writing is one with around 8-16Gb

### 5.1.2 Results

In Table 2, we list the training results recorded directly from the training process, while in Table 3, we list the inference results for the VMC experiments for the 1D TFIM at  $N = 20, 40, 80, 100$ . The inference results are obtained by using the trained models to generate new spin configurations to calculate the new NQS wavefunction. The convergence plots for the mean energy and energy variance recorded from the training process are shown in Fig.11 and Fig.12 in Appendix A.1.

Ansatz	$N = 20$	$N = 40$	$N = 80$	$N = 100$
eRNN-50-s50	-25.0842 (0.056)	-50.5988 (0.143)	-101.3826 (0.185)	<b>-126.9536</b> (0.377)
eGRU-50-s50	<b>-25.1067</b> (0.059)	-50.5396 (0.063)	<b>-101.5267</b> (0.133)	-126.9521 (0.142)
hGRU-50-s50	-25.1202 (0.054)	<b>-50.5615</b> (0.126)	-101.5501 (0.437)	-126.9738 (0.183)
Exact (DMRG)	-25.1078	-50.5694	-101.4974	-126.9619

Table 2: VMC training results for 1D TFIM Hamiltonian with various system sizes  $N = 20, 40, 80, 100$  for  $J = 1$  and  $B = 1$ . These results are recorded directly from the training process and correspond to the parameters of the best saved model. For each ansatz, the mean  $E$  is listed first, together with the variance (in brackets). The best training result for the converged mean energy at each  $N$  is noted in bold.

Ansatz	$N = 20$	$N = 40$	$N = 80$	$N = 100$
eRNN-50-s50	<b>-25.0802</b> (0.074)	<b>-50.5518</b> (0.248)	-101.3626 (0.331)	<b>-126.8852</b> (0.141)
eGRU-50-s50	-25.0713 (0.068)	-50.5922 (0.220)	-101.4369 (0.160)	-126.8455 (0.249)
hGRU-50-s50	-25.0725 (0.055)	-50.6399 (0.149)	<b>-101.4554</b> (0.481)	-126.7369 (0.245)
Exact (DMRG)	-25.1078	-50.5694	-101.4974	-126.9619

Table 3: VMC inference results for 1D TFIM Hamiltonian with various system sizes  $N = 20, 40, 80, 100$  for  $J = 1$  and  $B = 1$ . For each ansatz, the mean  $E$  is listed first, together with the variance (in brackets). These results are obtained from the inference process in which the trained parameters are loaded into new models and these models are used to calculate the mean energy. The best inference result for the converged mean energy at each  $N$  is noted in bold.

The results listed in Table 2 and Table 3 are graphically presented in Fig.4, from which one can see immediately the performances of the three types of NQS ansatzes with respect to one another. We note that it is not out of the ordinary that the performances during training and inference of the same ansatz differ.

1. For  $N = 20$ , the best NQS ansatz is eRNN-50-s50 (Euclidean RNN) from inference and eGRU-50-s50 (Euclidean GRU) from training.
2. For  $N = 40$ , the best NQS ansatz is eRNN-50-s50 (Euclidean RNN) from inference and hGRU-50-s50 (hyperbolic GRU) from training.
3. For  $N = 80$ , the best NQS ansatz is hGRU-50-s50 (hyperbolic GRU) from inference and eGRU-50-s50 (Euclidean GRU) from training.
4. For  $N = 100$ , the best NQS ansatz is eRNN-50-s50 (Euclidean RNN) from both inference and training. For the training process, the three NQS ansatzes have very close performances among one another.

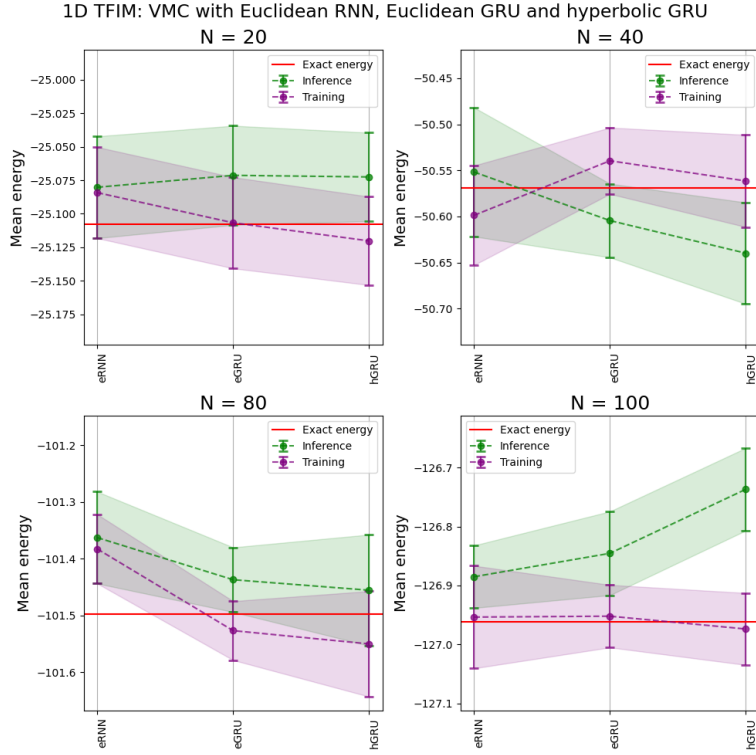


Figure 4: VMC experiments for 1D TFIM with  $N = 20, 40, 80$  and  $100$  spins (from top to bottom row, left to right): Comparisons of the performances of the variants eRNN-50-s50, eGRU-50-s50, hypGRU-50-s50 (listed in Table 1) - abbreviated as eRNN, eGRU and hGRU on the horizontal axis of each subfigure - during training and inference processes. In each subfigure, the mean energy from training and inference for each NQS ansatz is shown as a dot with error bar (representing the standard error).

## 5.2 2D Transverse Field Ising Model

In this section, we consider the two-dimensional transverse field Ising model on a square lattice with open boundary condition, with the following Hamiltonian

$$H = -J \sum_{\langle i,j \rangle} \sigma_z^i \sigma_z^j - B \sum_i \sigma_x^i \quad (51)$$

where the sum  $\langle i,j \rangle$  is over pairs of nearest-neighbor on the square 2D lattice. This system has a phase transition at the critical value of  $B_c = 3.044$  separating the magnetically ordered phase from a random paramagnet [39]. In our VMC experiments, as is the case in [9], we fix  $J = 1.0$  and  $B = 3.0$ .

### 5.2.1 Experiment details

For the 2D TFIM, we will perform the VMC experiments using three different NQS ansatzes: one-dimensional Euclidean GRU, one-dimensional hyperbolic GRU and two-dimensional Euclidean RNN, the details (including the names and number of parameters) of which are included in Table 4. The size  $(N_x, N_y)$  of the square lattice in the 2D TFIM is chosen to be  $(5,5)$ ,  $(7,7)$ ,  $(8,8)$  and  $(9,9)$ <sup>11</sup> corresponding to systems with 25, 49, 64 and 81 spins. All neural network ansatzes are real NQS wavefunction (described in Section 4.1) whose architecture comprises an RNN unit (either Euclidean GRU, hyperbolic GRU or 2D Euclidean RNN) with the hidden dimension  $d_h = 50$ , and a Dense layer with the Softmax activation function.

<sup>11</sup>Unfortunately, we do not have enough computing resources to carry out the VMC experiments for the case of  $(N_x, N_y) \geq (10, 10)$

Ansatz	Name	Parameters
1D Euclidean GRU	1d-eGRU-50-s50	8052
1D Hyperbolic GRU	1d-hGRU-50-s50	8052
2D Euclidean RNN	2d-RNN-50-s50	5352

Table 4: The variants of Euclidean and hyperbolic GRU used as NQS ansatzes to run the VMC experiments involving the 2D TFIM with  $(N_x, N_y) = (5, 5), (7, 7), (8, 8), (9, 9)$ , at  $J = 1$  and  $B = 3.0$ .

The 2D Euclidean RNN is a new custom construction from [9] with the following defining equation

$$\vec{h}_{t+1} = f \left( U_h \vec{x}_t^0 + W_h \vec{h}_t^0 + U_v \vec{x}_t^1 + W_v \vec{h}_t^1 + \vec{b} \right), \quad (52)$$

where  $f$  is a nonlinear activation function, the input  $\vec{x}_t = (\vec{x}_t^0, \vec{x}_t^1)$  and hidden state  $\vec{h}_t = (\vec{h}_t^0, \vec{h}_t^1)$  at timestep  $t$  are now a 2D vectors comprising the horizontal and vertical components. Correspondingly, there is a doubling of the usual weight matrices  $U$  and  $W$  to  $U_h, U_v, W_h, W_v$ . For a 2D spin configuration  $\sigma$  of dimension  $(N_x, N_y)$ , an entry  $s_{i,j}$  is autoregressively generated based on the two spins and two hidden states from its previously generated horizontal and vertical neighbors. For the 1D Euclidean/hyperbolic GRU, during the sampling process, the site  $\sigma_{i,j}$  is autoregressively generated based on only the previously generated site in a raster manner shown in Fig.5. At each time step  $t$  during the training phase, the 2D Euclidean RNN NQS ansatz generates 50 two-dimensional samples, each of which is a (2D) spin configuration (samples) of size  $(N_x, N_y)$ , while the 1D Euclidean/hyperbolic GRU ansatz generates 50 one-dimensional samples, each of which is a (1D) spin configuration of length  $N_x \times N_y$ . The computation of the energy for the 1D ansatz requires a reshaping of the 1D samples of length  $N_x \times N_y$  into 2D samples of size  $(N_x, N_y)$ .

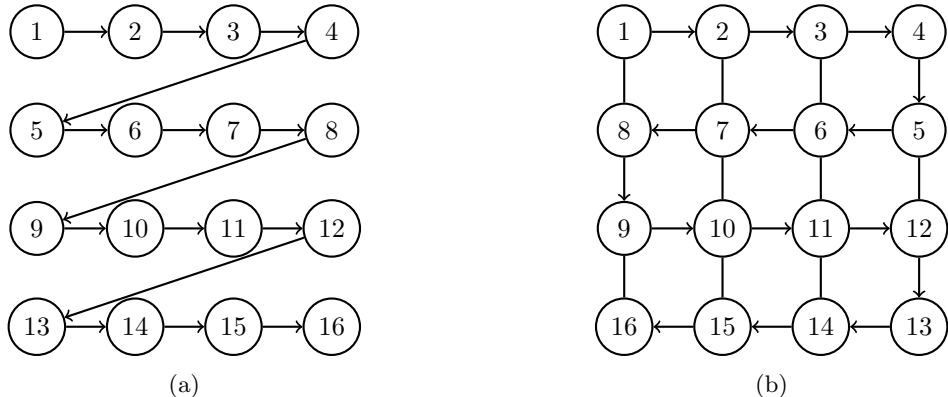


Figure 5: Schematic of the sampling process in the 2D TFIM model with a square lattice of size  $(N_x, N_y) = (4, 4)$  using (a) 1D Euclidean/hyperbolic GRU (b) 2D Euclidean RNN. The arrows in both (a) and (b) denote the autoregressive sampling path. For 2D RNN, each site in the square lattice receives 2 RNN hidden states from its nearest horizontal and vertical neighbors, while for 1D GRU, each site only receives the hidden state from its original nearest neighbor in the 1D chain. Figure adapted from [9].

Other training details are largely the same as described in the 1D TFIM, including the hardware configuration, the fixed (50) number of samples generated during training, the optimizer types (`Adam` for Euclidean NQS, with the learning rate of  $10^{-2}$  with exponential decay every 100 epochs, and a combination of `Adam`+`RSGD` for hyperbolic NQS where the learning rate setting is the same for `Adam` in the Euclidean case while for `RSGD`, it is a fixed learning rate of  $10^{-2}$  throughout) and the setup in which only the best model is saved during the training phase. For  $(N_x, N_y) = (5, 5), (7, 7)$ , with the number of training epochs being 450, 1D Euclidean GRU takes less than 2 hours, while 1D hyperbolic GRU takes up to 14 hours to finish the training. For  $(N_x, N_y) = (8, 8), (9, 9)$ , with the number of training epochs reduced 350 due to the significantly longer running time required, 1D Euclidean GRU takes around 4 hours, while 1D hyperbolic GRU can take up to around 30 hours to finish the training. For the lighter 2D Euclidean RNN that reaches convergence faster than the 1D ansatzes, the number of epochs varies and is 200 for  $(N_x, N_y) = (5, 5)$ , 300 for  $(N_x, N_y) = (7, 7)$  and 350 for  $(N_x, N_y) = (8, 8), (9, 9)$ . The training time of 2D Euclidean RNN ranges from 0.2 hour for  $(N_x, N_y) = (5, 5)$  to 3.5 hours for  $(N_x, N_y) = (9, 9)$ .

### 5.2.2 Results

The training and inference results for the VMC experiments involving the 2D TFIM setting are listed in Table 5 and Table 6. The convergence curve plots for the mean energy and energy variance are shown in Fig.13 and Fig.14 in Appendix A.2.

Ansatz	$(N_x, N_y) = (5, 5)$	$(N_x, N_y) = (7, 7)$	$(N_x, N_y) = (8, 8)$	$(N_x, N_y) = (9, 9)$
1d-eGRU-50-s50	-78.2474 (1.725)	-154.4191 (9.037)	-202.4174 (26.062)	-256.6143 (27.569)
1d-hGRU-50-s50	-78.7007 (1.905)	-154.6777 (4.757)	-203.0641 (26.092)	-256.5937 (29.217)
2d-eRNN-50-s50	<b>-78.7774</b> (0.194)	<b>-154.7002</b> (0.242)	<b>-202.8181</b> (1.041)	<b>-256.7666</b> (1.383)
DMRG	-78.6857	-154.8463	-202.5077	-256.5535

Table 5: VMC training results for 2D TFIM Hamiltonian with various system sizes  $(N_x, N_y)$  for  $J = 1$  and  $B = 3.0$ . These results are recorded directly from the training process and correspond to the parameters of the best saved model. For each ansatz, the mean  $E$  is listed first, together with the variance (in brackets). The best and second best results for the converged mean energy for each  $(N_x, N_y)$  case are noted in bold and typewriter font, respectively. For this 2D TFIM setting, we care more about the second best than the best result, since the best result in each case is expected to be 2D Euclidean RNN.

Ansatz	$(N_x, N_y) = (5, 5)$	$(N_x, N_y) = (7, 7)$	$(N_x, N_y) = (8, 8)$	$(N_x, N_y) = (9, 9)$
1d-eGRU-50-s50	-78.1900 (5.300)	-153.3293 (14.429)	-200.0871 (26.120)	-255.4191 (28.418)
1d-hGRU-50-s50	-78.3403 (4.480)	-154.4542 (7.054)	-200.5193 (28.783)	-255.6020 (19.538)
2d-eRNN-50-s50	<b>-78.6763</b> (0.390)	<b>-154.6495</b> (0.448)	<b>-202.3759</b> (1.083)	<b>-256.7026</b> (0.881)
DMRG	-78.6857	-154.8463	-202.5077	-256.5535

Table 6: VMC inference results for 2D TFIM Hamiltonian with various system sizes  $(N_x, N_y)$  for  $J = 1$  and  $B = 3.0$ . These results were obtained from the inference process in which the trained model is used to generate new spin configurations whose mean energies are then calculated. For each ansatz, the mean  $E$  is listed first, together with the variance (in brackets). The best and second best results for the converged mean energy for each  $(N_x, N_y)$  case are noted in bold and typewriter font, respectively. For this 2D TFIM setting, we care more about the second best than the best result, since the best result in each case is expected to be 2D Euclidean RNN.

From Table 5, Table 6 and Fig.6, it is clear that 2D Euclidean RNN is the best performing ansatz in all four cases for both training and inference, since the architecture of the RNN part of this NQS was specially created for the 2D setting of TFIM. It is thus within our expectation that 2D RNN will outperform both 1D Euclidean and hyperbolic GRU. What we are really interested in, and would like to find out, however, is whether 1D hyperbolic GRU will outperform 1D Euclidean GRU. Regarding this aspect, we observe that in the training process, hyperbolic GRU outperform Euclidean GRU 3 out of 4 times when  $(N_x, N_y) = (5, 5), (7, 7), (9, 9)$ , while in inference process, hyperbolic GRU outperform Euclidean GRU 4 out of 4 times (see Fig.6). While for  $(N_x, N_y) = (5, 5), (7, 7)$ , it is clear that hyperbolic GRU definitively outperform Euclidean GRU for in both training and inference, the situation is not clear-cut for  $(N_x, N_y) = (8, 8), (9, 9)$ . When  $(N_x, N_y) = (9, 9)$  Euclidean and hyperbolic GRU are almost comparable in performance during training, while for  $N_x, N_y) = (8, 8)$ , their inference results are almost comparable, although for both cases, hyperbolic GRU still emerged as the slightly better variant. Also, from the converge curve for the mean energy, Fig.13, we note that the cyan curve corresponding to 1D hyperbolic GRU is always closer, with narrower range of fluctuations, to the DMRG line than the blue curve corresponding to 1D Euclidean GRU, even for the case of  $(N_x, N_y) = (8, 8)$ , when the final saved 1D hyperbolic GRU model does not yield the result as good as that of 1D Euclidean GRU (see the first subfigure on the second row of Fig.13). While more experiments are needed, especially for larger  $(N_x, N_y)$  sizes, from the results of these experiments, it can be seen that 1D hyperbolic GRU is likely to outperform 1D Euclidean GRU.

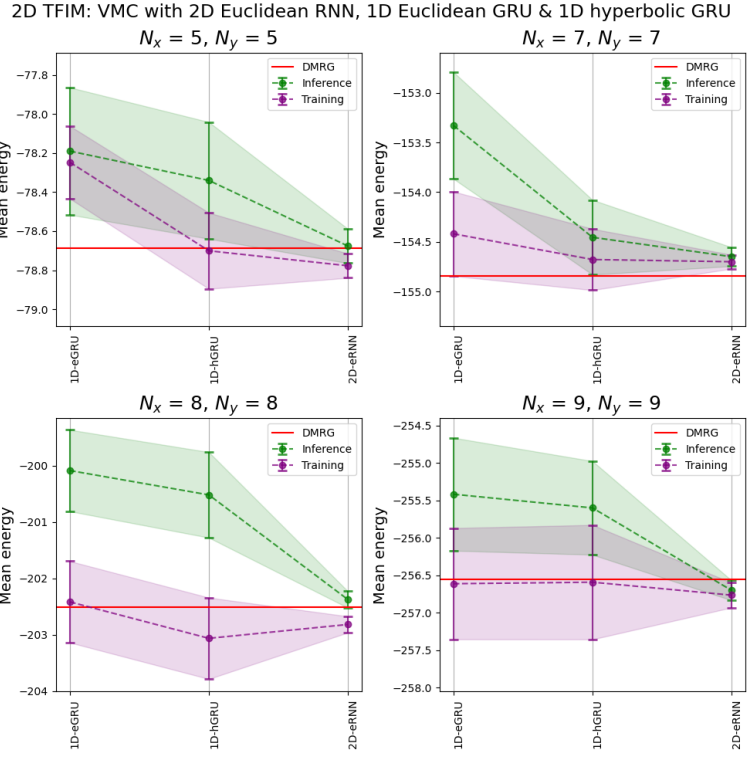


Figure 6: Comparisons of the performances (during training and inference) of 2D Euclidean RNN and 1D Euclidean/hyperbolic GRU ansatzes listed in Table 4 for the 2D TFIM with different  $(N_x, N_y)$  lattices - clockwise from top:  $(N_x, N_y) = (5, 5), (7, 7), (9, 9), (8, 8)$ . Each dot with error bar represents the mean  $E$  value of an NQS ansatz. For all cases, 2D Euclidean RNN is the best ansatz. The second best ansatz is 1D hyperbolic GRU for all cases, except for the training result of  $(N_x, N_y) = (8, 8)$ .

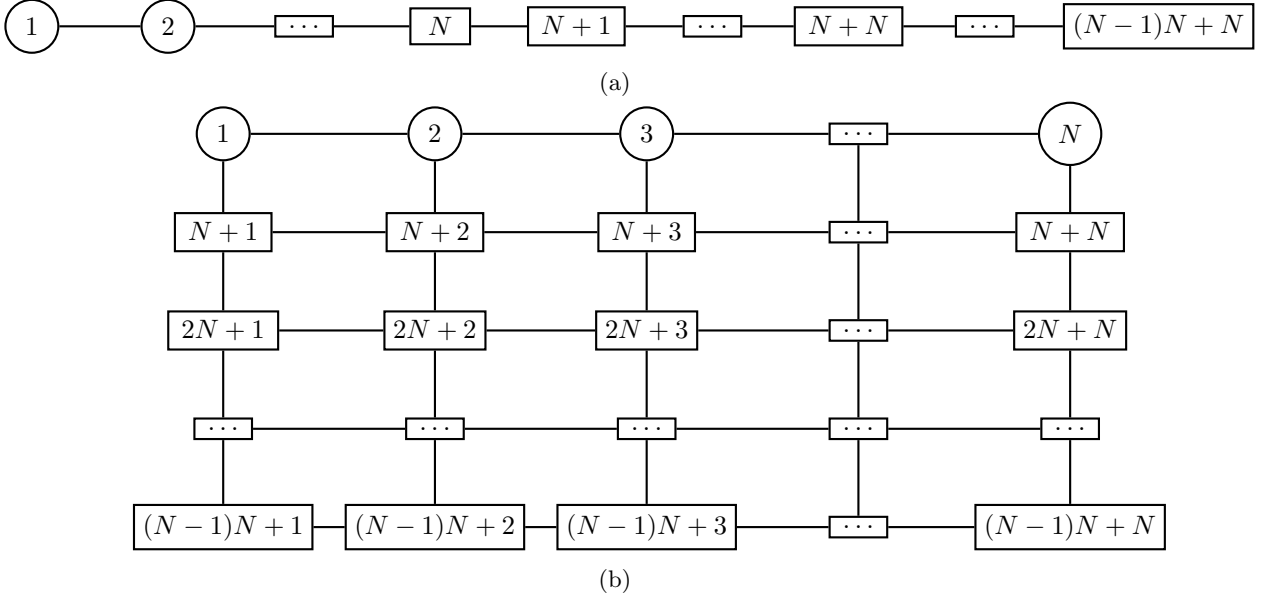


Figure 7: The process of rearranging or reshaping a 1D chain of length  $N^2 = (N-1)N + N$  into a 2D lattice  $N \times N$  introduces additional interactions between site  $i$  and site  $(i+N)$  when the vertical dimension is ‘formed’. (a) The original 1D chain with length  $N^2 = (N-1)N + N$ , with each site in the chain labeled by their 1D position. (b) The same 1D chain of length  $N^2 = (N-1)N + N$  rearranged in a 2D square lattice of size  $N \times N$ , with each site in the square lattice labeled by their original 1D position.

This result is very interesting since it might be indicative of the role played by the hyperbolic geometry of the NQS ansatz in Hamiltonian systems where there exist some sort of hierarchical structure. In the context of natural language processing (NLP) when the hyperbolic RNN/GRU was introduced in the work of [30],

the authors noted a definitive and clear outperformance of hyperbolic RNN/GRU over their Euclidean version when the underlying data exhibit a hierarchical, tree-like structure. In the present 2D TFIM setting, there exists a hierarchy in the interaction structure of 2D Hamiltonian when 1D NQS is used. This is due to the artificial rearrangement (or folding) of the 1D samples generated by the 1D NQS into 2D samples during the calculations of their local energies (see Fig.7). This process of rearrangement creates additional interactions between neighbors at site  $i$  and site  $i + N$ , which were originally faraway in the 1D horizontal chain but are brought close together to form the vertical dimension in the 2D square lattice. Concretely, let us consider a chain of length  $N^2 = (N - 1)N + N$  spins (see Subfigure (a) of Fig.7) folded into a square lattice of size  $(N, N)$  in Subfigure (b) of Fig.7. In 1D when only the next nearest neighbor interactions are counted, site  $i$  and site  $i + N$  have no interaction, but when arranged in a 2D square lattice, these sites are each other next nearest neighbor vertically, which means their interactions are counted in the local energy calculations. Together with the original 1D next nearest neighbor interactions  $\langle i, i + 1 \rangle$ , these additional interactions  $\langle i, i + N \rangle$  actually form a hierarchy of interactions<sup>12</sup>, and it is this hierarchy that might have played a part in the observation of 1D hyperbolic GRU outperforming 1D Euclidean GRU in 2D TFIM setting.

### 5.3 1D Heisenberg $J_1 J_2$ Model

The Hamiltonian of the one-dimensional  $J_1 J_2$  model is

$$H_{J_1-J_2} = J_1 \sum_{\langle i,j \rangle} S_i \cdot S_j + J_2 \sum_{\langle\langle i,j \rangle\rangle} S_i \cdot S_j \quad (53)$$

The  $S_i = S_x, S_y, S_z$  are the spin-half operators (Pauli matrices). The first sum with the coefficient  $J_1$  in the Hamiltonian is over pairs of nearest neighbors while the second sum with the coefficient  $J_2$  is over pairs of next nearest neighbors. When  $J_2 = 0$ , only nearest neighbor interactions are counted while next nearest neighbor interactions are switched off. It is known that from DMRG studies that this 1D model exhibits a phase transition at the critical  $J_2$  value of  $J_2^c = 0.2412 \pm 0.000005$  from a critical Luttinger liquid phase ( $J_2 \leq J_2^c$ ) to a spontaneously gapped valence bond state phase ( $J_2 \geq J_2^c$ ) [9], [44], [45], [46]. When  $J_2 = 0.5$ , the 1D  $J_1 J_2$  model reduce to the Majumdar-Ghosh model.

#### 5.3.1 Experiment details

For the 1D  $J_1 J_2$  system with  $J_1 = 1.0$  and  $J_2 = 0.0, 0.2, 0.5, 0.8$ , we carried out several VMC experiments using Euclidean and hyperbolic GRU NQS in the form of the complex NQS wavefunction Eq.(45) described in 4.2. The architecture of these neural networks consist of a Euclidean/hyperbolic RNN unit and two Dense layers with 2 units each, one with the Softmax activation and one with the Softsign activation. Furthermore, making use of the observation from [9] that reported an improvement in the final results when the Marshall sign [47] is used, the wavefunction can be written as

$$\Psi(\vec{\sigma}) = (-1)^{M_A(\vec{\sigma})} \tilde{\Psi}(\vec{\sigma}) \quad (54)$$

where  $M_A(\vec{\sigma}) = \sum_{i \in A} \sigma_i$ , and  $\tilde{\Psi}(\sigma)$  is the positive amplitude of the wavefunction, with  $A$  comprising the sites belonging to the sublattice of all even or all odd sites in the lattice. The factor  $(-1)^{M_A(\vec{\sigma})}$  is the Marshall sign of the wavefunction, and Eq.(54) holds true when  $J_2 = 0$ . When  $J_2 \neq 0$ , Eq.(54) is no longer exact but still holds approximately [7].

In all VMC experiments, the same Euclidean GRU variant, **eGRU-75-s50**, with the RNN hidden dimension  $d_h = 75$  and 17854 trainable parameters<sup>13</sup> is used to establish a benchmark performance against which we compare the performances of different variants of hyperbolic GRU. In particular, for each  $J_2$  value, three variants of hyperbolic GRU with the RNN hidden dimension of  $d_h = 60, 70, 75$  (**hGRU-60-s50**, **hGRU-70-s50**, **hGRU-75-s50**) were considered and used to run the VMC experiments, and the best result among these variants<sup>14</sup> is selected to compare with the benchmark result provided by the Euclidean GRU. The list of all Euclidean/hyperbolic GRU variants is listed in Table 7.

<sup>12</sup>Note that alongside the gained interaction  $\langle i, i + N \rangle$ , we also lose some next nearest neighbor interactions  $\langle i, i + 1 \rangle$  when  $i = kN$ , with  $k \in \mathbb{N}$ , i.e. when  $i$  is multiple of  $N$

<sup>13</sup>As a passing remark, we note that in the work [9], the authors used a much larger GRU-based model, comprising three layers of GRU, each with  $d_h = 100$  to approximate the ground state energy of the 1D  $J_1 J_2$  model with  $N = 100$  spins. Their goal was to establish the performance of GRU-based neural network as an effective NQS. Here we are interested in establishing the performance of the hyperbolic version of the GRU-based NQS and not its Euclidean counterpart. This, and the fact that our 1D  $J_1 J_2$  system has a smaller number of spins  $N$  ( $N = 50$  instead of 100), motivates our choice of using a smaller Euclidean GRU-based NQS.

<sup>14</sup>Sometimes a variant with smaller  $d_h$  hidden units outperforms one with larger  $d_h$ , as is the case for  $J_2 = 0.0, 0.5$  when **hGRU-60-s50** and **hGRU-70-s50** outperform **hGRU-75-s50**, which ran into the problem of overfitting during the training process.

Ansatz	$J_2 = 0.0$	$J_2 = 0.2$	$J_2 = 0.5$	$J_2 = 0.8$
Euclidean GRU Parameters	eGRU-75-s50 17854	eGRU-75-s50 17854	eGRU-75-s50 17854	eGRU-75-s50 17854
Hyperbolic GRU Parameters	hGRU-60-s50 11584	hGRU-75-s50 17854	hGRU-70-s50 15614	hGRU-75-s50 17854

Table 7: The variants of Euclidean and hyperbolic GRU used as NQS ansatzes to run the VMC experiments involving the 1D  $J_1 J_2$  Hamiltonian Eq.(53) with  $N = 50$ ,  $J_1 = 1$  and  $J_2 = 0.0, 0.2, 0.5, 0.8$ . While three variants of hyperbolic GRU with  $d_h = 60, 70, 75$  were used in the experiments, we only list the best performing variant in this Table. The second and last rows titled ‘Parameters’ list the numbers of parameters in the Euclidean and hyperbolic GRU networks.

Aside from the fact that the wavefunction in this case is complex instead of real, the other training details (the type of optimizers used, the training method in which only the best model is saved, and the hardware platform) remain exactly the same as described in the 1D TFIM case. The number of training epochs are 450 for  $J_2 = 0.0, 0.2$  and 400 for  $J_2 = 0.5, 0.8$ . As is the case in the 1D TFIM setting, hyperbolic GRU takes 5-7 times longer to complete the training loop than Euclidean GRU due to their more involved mathematical construction<sup>15</sup>.

### 5.3.2 Results

In Table 8 we list the results recorded during the training process and in Table 9 we list the results obtained by performing the inference process in which the trained models are used to generate new samples to calculate new NQS wavefunction. Fig.8 graphically represent the data in both Tables 8, 9 and show the comparison of the performances between Euclidean and hyperbolic GRU for all four values of  $J_2$ . The convergence curve plots for the mean energy and energy variance recorded during the training process are shown in Fig.15 and Fig.16, respectively, in Appendix A.3. Unlike the smooth convergence curves of the 1D TFIM case, the training in this case is less stable with multiple kinks in the energy convergence curves (see Fig.15) as well as multiple spikes in the variance convergence curves (Fig.16).

Ansatz	$J_2 = 0.0$	$J_2 = 0.2$	$J_2 = 0.5$	$J_2 = 0.8$
Euclidean GRU	<b>-21.3965</b> (0.57)	-17.4711 (1.64)	-17.4876 (0.5)	-19.6381 (0.71)
Hyperbolic GRU	-20.6559 (0.71)	<b>-20.0590</b> (0.71)	<b>-18.7244</b> (0.9)	<b>-20.1820</b> (0.83)
Exact (DMRG)	-21.9721	-20.3150	-18.7500	-20.9842

Table 8: VMC training results for the 1D  $J_1 J_2$  system with the Hamiltonian Eq.(53) with  $N = 50$ ,  $J_1 = 1$  and  $J_2 = 0.0, 0.2, 0.5, 0.8$ . For each ansatz, the mean  $E$  is listed first, together with the variance (in brackets). The best result at each  $J_2$  value is noted in bold.

Ansatz	$J_2 = 0.0$	$J_2 = 0.2$	$J_2 = 0.5$	$J_2 = 0.8$
Euclidean GRU	<b>-21.2575</b> (0.59)	-17.7340 (2.05)	-17.3381 (0.63)	-19.3249 (2.02)
Hyperbolic GRU	-20.3342 (0.75)	<b>-19.9232</b> (0.58)	<b>-18.4635</b> (0.58)	<b>-20.1790</b> (1.05)
Exact (DMRG)	-21.9721	-20.3150	-18.7500	-20.9842

Table 9: VMC inference results for the 1D  $J_1 J_2$  system with the Hamiltonian Eq.(53) with  $N = 50$ ,  $J_1 = 1$  and  $J_2 = 0.0, 0.2, 0.5, 0.8$ . For each ansatz, the mean  $E$  is listed first, together with the variance (in brackets). The best result at each  $J_2$  value is noted in bold.

From Table 8, Table 9 and Fig.8, we note that in both training and inference, hyperbolic GRU outperform Euclidean GRU on 3 out of 4 cases. In particular, these 3 cases all correspond to nonzero values of  $J_2$ , i.e. when  $J_2 = 0.2, 0.5, 0.8$ , in which the next nearest neighbor interactions are taken into account. When  $J_2 = 0.0$  (only nearest interactions - no next nearest neighbor interactions), Euclidean GRU outperform hyperbolic GRU (in

<sup>15</sup>For  $J_2 = 0$ , Euclidean GRU takes around 2.7 hours to complete the training, while for  $J_2 \neq 0$ , Euclidean GRU takes around 4 hours to complete the training on an average laptop with no GPU

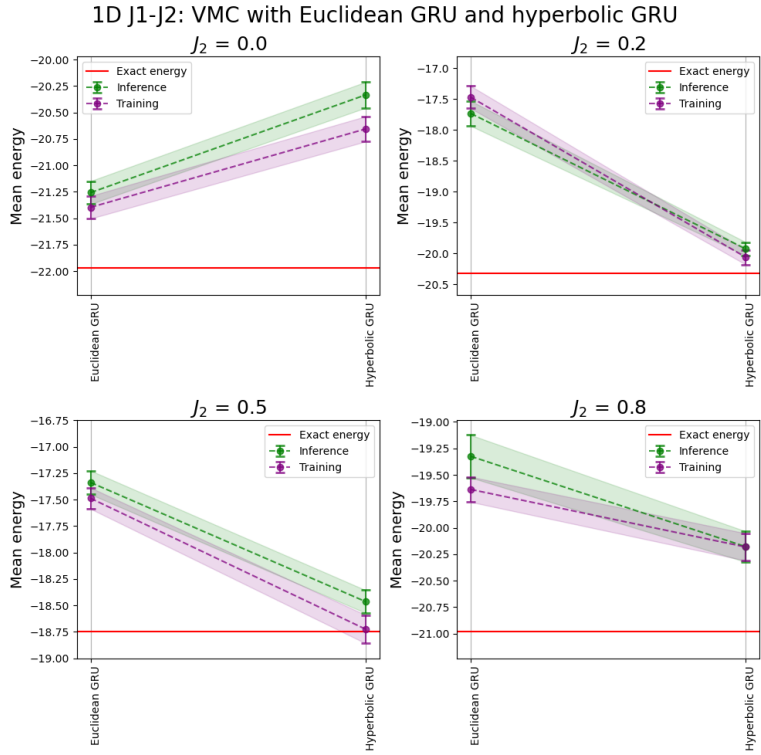


Figure 8: Comparisons of the performances of Euclidean and hyperbolic GRU NQS ansatzes listed in Table 7 from VMC runs of 1D  $J_1J_2$  model with different  $J_2$  values (clockwise from top:  $J_2 = 0.0, 0.2, 0.8, 0.5$ ) for  $N = 50$  spins. In each subfigure, the mean energy and standard error from training and inference for each NQS ansatz is shown as a dot with error bar. The specific variants of Euclidean/hyperbolic GRU used in each of the four cases are listed in Table 7. In this plot, we do not specify the exact variants, but label them simply as Euclidean GRU or hyperbolic GRU to emphasize the geometry of the ansatzes.

both training and inference). This result is again very interesting in the sense that it might be again indicative of the connection between the geometry of the NQS ansatz used and the structure of the Hamiltonian system under study, similar to the 2D TFIM setting above in which we observe a clear trend of outperformance by 1D hyperbolic GRU compared to 1D Euclidean GRU when there is a hierarchy in the Hamiltonian interaction structure, comprising the first and  $N^{th}$  nearest neighbor interactions, introduced by the artificial rearrangement of the 1D spin chain to mimic the 2D spin lattice. In this case, when second nearest neighbor interactions are switched on ( $J_2 > 0$ ), there is also a hierarchy going from the first nearest to the second nearest interactions, and it is our hypothesis that it is the decisive factor that leads to the outperformance of the hyperbolic GRU-based NQS over its Euclidean counterpart. It is unclear to us at the moment, although it is within our expectation, whether this would still be the case in two dimensions, i.e. whether hyperbolic GRU NQS carries on outperforming Euclidean GRU NQS in 2D  $J_1J_2$  models with different 2D lattice geometries (such as square, triangle, kagome, etc.). In order to perform the VMC experiments for 2D  $J_1J_2$  systems, one first needs to generalize the 1D hyperbolic GRU part of the NQS to two dimensions, similar to what was done in [9] in generalizing the 1D Euclidean RNN cell to its 2D version in Eq.(52).

## 5.4 1D Heisenberg $J_1J_2J_3$ Model

The Hamiltonian of the one-dimensional Heisenberg  $J_1J_2J_3$  model is

$$H_{J_1J_2J_3} = J_1 \sum_{\langle i,j \rangle} S_i \cdot S_j + J_2 \sum_{\langle\langle i,j \rangle\rangle} S_i \cdot S_j + J_3 \sum_{\langle\langle\langle i,j \rangle\rangle\rangle} S_i \cdot S_j \quad (55)$$

where  $S_i = S_x, S_y, S_z$  are the spin-half operators (Pauli matrices). The first sum with the coefficient  $J_1$  in the Hamiltonian is over pairs of nearest neighbors, the second sum with the coefficient  $J_2$  is over pairs of second nearest neighbors, and the third sum with the coefficient  $J_3$  is over pairs of third nearest neighbors. When both  $J_2 \neq 0$  and  $J_3 \neq 0$ , this model has a complicated phase transition properties that depend almost entirely on the relative strength of the competing  $J_2$  and  $J_3$  interactions [48]. Compared to the  $J_1J_2$  model, the  $J_1J_2J_3$  model is studied much less frequently in the literature, and even more so for the case of the one-dimensional  $J_1J_2J_3$  model, but it is believed that the  $J_3$  interactions in the 1D model between third nearest neighbors are relevant for describing the magnetic properties of quasi one-dimensional edge-shared cuprates such as LiVCuO<sub>4</sub> or LiCu<sub>2</sub>O<sub>2</sub> [48].

### 5.4.1 Experiment details

For the 1D Heisenberg  $J_1J_2J_3$  model with open boundary condition, we will carry out the VMC experiments with the number of spins  $N = 30$  using the following four settings (with  $J_1 = 1.0$ ):

1.  $(J_2, J_3) = (0.0, 0.5)$ : No second neighbor interactions, the  $J_1J_2J_3$  model reduces to  $J_1J_3$  model with only first and third nearest neighbor interactions.
2.  $(J_2, J_3) = (0.2, 0.2)$ : Second and third neighbor interactions have the same strength.
3.  $(J_2, J_3) = (0.2, 0.5)$ : Second neighbor interactions are stronger than third neighbor interactions.
4.  $(J_2, J_3) = (0.5, 0.2)$ : Second neighbor interactions are weaker than third neighbor interactions.

The NQS used are the complex Euclidean GRU and hyperbolic GRU ansatzes as in the 1D  $J_1J_2$  case. We will perform two different sets of VMC experiments.

- In the first set of experiments, all four  $(J_2, J_3)$  cases listed above are considered, withnthe Euclidean/hyperbolic GRU NQS ansatzes used having the same RNN hidden dimension of  $d_h = 50$  (see Table 10 for the variant names and their numbers of parameters).

$(J_2, J_3)$	Euclidean GRU	Hyperbolic GRU
(0.0, 0.5)		
(0.2, 0.2)	eGRU-50-s50	hGRU-50-s50
(0.2, 0.5)	(8154)	(8154)
(0.5, 0.2)		

Table 10: The variants of Euclidean and hyperbolic GRU used as NQS ansatzes to run the first set of VMC experiments involving the 1D  $J_1J_2J_3$  Hamiltonian Eq.(55) with  $N = 30$ ,  $J_1 = 1$  and  $(J_2, J_3) = (0.0, 0.5), (0.2, 0.2), (0.2, 0.5), (0.5, 0.2)$ . The number of parameters of each NQS is listed in brackets under their names. Only one variant for each type of NQS ansatz is used in this set of VMC experiments.

- In the second set of experiments, we only considered  $(J_2, J_3) = (0.2, 0.5), (0.5, 0.2)$ , with the Euclidean GRU ansatz having the RNN hidden dimension  $d_h = 60$  and the hyperbolic GRU ansatz having  $d_h = 55$  (see Table 11).

In the first set of VMC experiments, we only use one variant each for either Euclidean (eGRU-50-s50 with  $d_h = 50$ ) or hyperbolic GRU (hGRU-50-s50 with  $d_h = 50$ ) and fix the number of training epochs to 280 in all cases. In the second set of VMC experiments, we explore the performances of hyperbolic GRU variants with  $d_h = 53, 55, 57$  to choose the best one among them to compare with the Euclidean GRU benchmark, eGRU-60-s50 with  $d_h = 60$ , while extending the number of training epochs to 350 for  $(J_2, J_3) = (0.2, 0.5)$  and 500 for  $(J_2, J_3) = (0.5, 0.2)$ . Similar to previous cases, in each experiment, hyperbolic GRU can take up to around 5 times longer to complete the training (on the same hardware) than Euclidean GRU with the same  $d_h$ <sup>16</sup>. All other training details (optimizer settings, saving-of-best-model-only method) remain the same as in the 1D  $J_1J_2$  case and will not be repeated here.

<sup>16</sup>while hyperbolic GRU with smaller  $d_h$  also takes longer to train, up to around 2-3 times, than Euclidean GRU with larger  $d_h$

$(J_2, J_3)$	Euclidean GRU	Hyperbolic GRU
(0.2, 0.5)	eGRU-60-s50 (11584)	hGRU-55-s50 (9794)
(0.5, 0.2)	eGRU-60-s50 (11584)	hGRU-57-s50 (10492)

Table 11: The variants of Euclidean and hyperbolic GRU used as NQS ansatzes to run the second set of VMC experiments involving the 1D  $J_1 J_2 J_3$  Hamiltonian Eq.(55) with  $N = 30$ ,  $J_1 = 1$  and  $(J_2, J_3) = (0.2, 0.5), (0.5, 0.2)$ . Only one variant of Euclidean GRU, eGRU-60-s50 with  $d_h = 60$  was used. Three variants of hyperbolic GRU with  $d_h = 53, 55, 57$  were used in the experiment, but we only list the best performing variant in this Table. The number of parameters of each NQS is listed in brackets under their names.

#### 5.4.2 Results

- For the first set of VMC experiments involving  $(J_2, J_3) = (0.0, 0.5), (0.2, 0.2), (0.2, 0.5), (0.5, 0.2)$  with the NQS ansatzes listed in Table 10, the training and inference results are listed in Table 12 and Table 13, respectively. Fig.9 graphically shows the data in both these Tables and offers a comparison between the performances of the 1D Euclidean and 1D hyperbolic GRU. The convergence curve plots for the mean energy and energy variance recorded during the training process are shown in Fig.17 and Fig.18, respectively, in Appendix A.4.

Ansatz	$(J_2, J_3) = (0.0, 0.5)$	$(J_2, J_3) = (0.2, 0.2)$	$(J_2, J_3) = (0.2, 0.5)$	$(J_2, J_3) = (0.5, 0.2)$
Euclidean GRU	11.47924 (1.113)	-10.93928 (0.904)	-10.07423 (2.860)	-9.78728 (1.368)
Hyperbolic GRU	<b>-15.1557</b> (1.690)	<b>-12.2377</b> (0.659)	<b>-12.9018</b> (0.4532)	<b>-10.954</b> (0.3374)
Exact (DMRG)	-15.89028	-12.9430	-14.64083	-11.52874

Table 12: VMC training results (from the first set of experiments with the NQS ansatzes listed in Table 10) for the 1D  $J_1 J_2 J_3$  system with the Hamiltonian Eq.(55) with  $N = 30$ ,  $J_1 = 1$ , and  $(J_2, J_3) = (0.0, 0.2), (0.2, 0.2), (0.2, 0.5), (0.5, 0.2)$ . These results are recorded directly from the training and correspond to the parameters of the best saved model. For each ansatz, the mean  $E$  is listed first, together with the variance (in brackets). The best result at each  $(J_2, J_3)$  case is noted in bold.

Ansatz	$(J_2, J_3) = (0.0, 0.5)$	$(J_2, J_3) = (0.2, 0.2)$	$(J_2, J_3) = (0.2, 0.5)$	$(J_2, J_3) = (0.5, 0.2)$
Euclidean GRU	-11.3272 (0.002)	-10.7929 (0.908)	-9.9025 (0.001)	-9.74123 (1.547)
Hyperbolic GRU	<b>-15.2398</b> (3.904)	<b>-12.2060</b> (2.976)	<b>-12.6666</b> (0.487)	<b>-10.7659</b> (0.157)
Exact (DMRG)	-15.8903	-12.9430	-14.6408	-11.5287

Table 13: VMC inference results (from the first set of experiments with the NQS ansatzes listed in Table 10) for the 1D  $J_1 J_2 J_3$  system with the Hamiltonian Eq.(55) with  $N = 30$ ,  $J_1 = 1$ , and  $(J_2, J_3) = (0.0, 0.2), (0.2, 0.2), (0.2, 0.5), (0.5, 0.2)$ . For each ansatz, the mean  $E$  is listed first, together with the variance (in brackets). The best result at each  $(J_2, J_3)$  case is noted in bold.

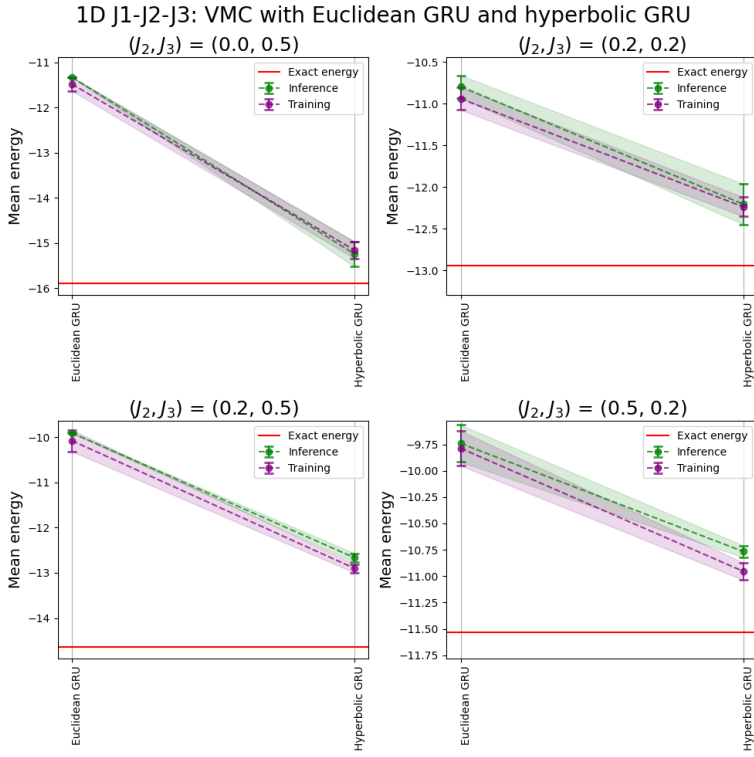


Figure 9: Comparisons of the performances of Euclidean and hyperbolic GRU NQS ansatzes listed in Table 10 from VMC runs of 1D  $J_1 J_2 J_3$  model with different  $(J_2, J_3)$  values - clockwise from top:  $(0.0, 0.5)$ ,  $(0.2, 0.2)$ ,  $(0.5, 0.2)$ ,  $(0.2, 0.5)$  - for  $N = 30$  spins. In each subfigure, the mean energy and standard error from training and inference for each NQS ansatz is shown as a dot with an error bar. As is the  $J_1 J_2$  case, we do not specify the exact variants (listed in Table 10) in this plot, but choosing instead to label them as ‘Euclidean GRU’ and ‘Hyperbolic GRU’ to emphasize the geometry of the NQS ansatz.

From Table 12, Table 13 and Fig.9, we note that in both training and inference, hyperbolic GRU definitively outperformed Euclidean GRU (by a large margin) in all 4 out of 4 cases. The energy convergence curves (see Fig.17) corresponding to the hyperbolic GRU ansatz reach convergence at values well below that reached by the curves corresponding to the Euclidean GRU ansatz, while the variance convergence curves of hyperbolic GRU (see Fig.18) show smaller ranges of fluctuations than Euclidean GRU’s.

- For the second set of VMC experiments involving only  $(J_2, J_3) = (0.2, 0.5), (0.5, 0.2)$  with the NQS ansatzes listed in Table 11, the training and inference results are included in Table 14 and Table 15. The comparison of the performances of hyperbolic and Euclidean GRU ansatzes is shown in Fig.10. The convergence curve plots of the second set of VMC experiments for the mean energy and energy variance recorded during the training process are shown in Fig.19 and Fig.20, respectively, in Appendix A.4.

Ansatz	$(J_2, J_3) = (0.2, 0.5)$	$(J_2, J_3) = (0.5, 0.2)$
Euclidean GRU	-14.8879 (1.135)	-11.4706 (0.113)
Hyperbolic GRU	<b>-14.6645</b> (1.344)	<b>-11.5146</b> (2.536)
Exact (DMRG)	-14.6408	-11.5287

Table 14: VMC training results (from the second set of experiments with the NQS ansatzes listed in Table 11) for the 1D  $J_1 J_2 J_3$  system with the Hamiltonian Eq.(55) with  $N = 30$ ,  $J_1 = 1$ , and  $(J_2, J_3) = (0.2, 0.5), (0.5, 0.2)$ . These results are recorded directly from the training and correspond to the parameters of the best saved model. For each ansatz, the mean  $E$  is listed first, together with the variance (in brackets). The best result at each  $(J_2, J_3)$  case is noted in bold.

From Table 14, Table 15 and Fig.10, for  $(J_2, J_3) = (0.2, 0.5)$ , the hyperbolic GRU ansatz **hGRU-55-s50** outperforms the Euclidean GRU ansatz **eGRU-60-s50** in the training process, as is evidence from the closer mean energy value obtained during training, as well as from the energy convergence curve shown in the first subfigure of Fig.19, which shows the curve corresponding to **hGRU-55-s50** reaching convergence faster

Ansatz	$(J_2, J_3) = (0.2, 0.5)$	$(J_2, J_3) = (0.5, 0.2)$
Euclidean GRU	<b>-14.6828</b> (1.000)	-11.2061 (0.403)
Hyperbolic GRU	-14.4243 (0.640)	<b>-11.3070</b> (0.065)
Exact (DMRG)	-14.6408	-11.5287

Table 15: VMC inference results (from the second set of experiments with the NQS ansatzes listed in Table 11) for the 1D  $J_1 J_2 J_3$  system with the Hamiltonian Eq.(55) with  $N = 30$ ,  $J_1 = 1$ , and  $(J_2, J_3) = (0.2, 0.5), (0.5, 0.2)$ . For each ansatz, the mean  $E$  is listed first, together with the variance (in brackets). The best result at each  $(J_2, J_3)$  case is noted in bold.

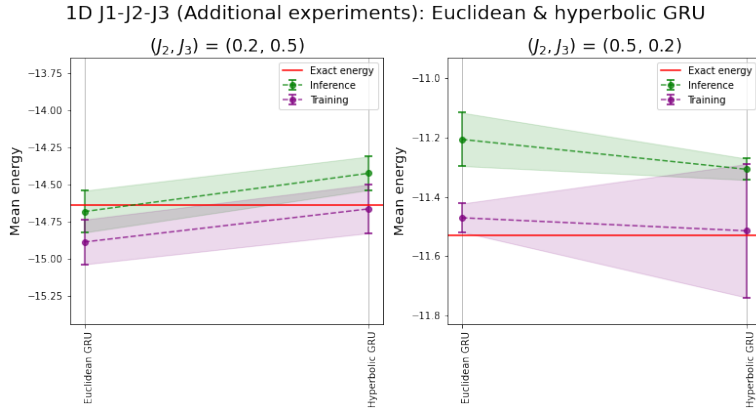


Figure 10: Comparisons of the performances of Euclidean and hyperbolic GRU NQS ansatzes listed in Table 11 from VMC runs of 1D  $J_1 J_2 J_3$  model with different  $(J_2, J_3)$  values - from left to right:  $(0.2, 0.5), (0.5, 0.2)$  - for  $N = 30$  spins. In each subfigure, the mean energy and standard error from training and inference for each NQS ansatz is shown as a dot with an error bar. As before, we do not specify the exact variants (listed in Table 11) in this plot, but choosing instead to label them as ‘Euclidean GRU’ and ‘Hyperbolic GRU’ to emphasize the geometry of the NQS ansatz.

with a narrower fluctuation range than the curve corresponding to eGRU-60-s50. In this case, it must be noted that the Euclidean GRU ansatz used, eGRU-60-s50, has around 20 percent more parameters (11584 versus 9794) than the hyperbolic GRU ansatz, hGRU-55-s50. For  $(J_2, J_3) = (0.5, 0.2)$ , the hyperbolic GRU ansatz hGRU-57-s50 outperforms the Euclidean GRU ansatz eGRU-60-s50 in both the training and inference processes. In this case, hyperbolic GRU has 10 percent fewer parameters than Euclidean GRU (10492 versus 11584).

From the two sets of VMC experiments for the 1D  $J_1 J_2 J_3$  model, we observe that the obtained results showing that hyperbolic GRU almost always outperform Euclidean GRU are in agreement with the ones in the 1D  $J_1 J_2$  case in which hyperbolic GRU outperformed its Euclidean version in all cases when  $J_2 \neq 0$ , i.e. when the second neighbor interaction is nonvanishing and the Hamiltonian exhibits a hierarchy in the interaction structure comprised of the first and second neighbor interactions. In all four  $J_1 J_2 J_3$  settings where there exist an even more pronounced hierarchy in the interaction structure of the Hamiltonian that comprises the first, second and third nearest neighbor interactions, the clear outperformance of the hyperbolic GRU ansatz reinforces the hypothesis that the hyperbolic geometry of this neural network plays a determining role in handling the type of Hamiltonians with hierarchical structures such as the 1D  $J_1 J_2$ ,  $J_1 J_2 J_3$  systems. As already noted in the 1D  $J_1 J_2$  case, an interesting task would be to verify whether hyperbolic GRU carries on outperforming Euclidean GRU for the 2D  $J_1 J_2 J_3$  models on different lattice geometries, but this will require the generalization of the 1D hyperbolic GRU network to a 2D version, similar to the generalization of the 1D Euclidean RNN cell to the 2D version in Eq.52 as done in [9].

## 6 Concluding remarks

In this work, we introduce the hyperbolic GRU as the first type of non-Euclidean neural quantum state (NQS) to be used in the variational Monte Carlo method (VMC) to approximate the ground state energy in quantum many-body physics, which are represented by the prototypical settings of the one-dimensional & two-dimensional transverse field Ising model (1D/2D TFIM) and the one-dimensional Heisenberg  $J_1J_2$  &  $J_1J_2J_3$  models. Our results show an interesting trend regarding the performance of the hyperbolic GRU as benchmarked against the performances of its Euclidean counterpart. In particular, using either the direct training or inference results, we note the following.

- In the 1D TFIM setting, with the number of spins  $N$  being 20, 40, 80 and 100, where the Hamiltonian comprises only the nearest neighbor interaction and a transverse magnetic field, with no hierarchical interaction structure, three out of four times, hyperbolic GRU does not outperform either Euclidean RNN or GRU.
- In the 2D TFIM setting, with the number of size of the 2D square lattice  $(N_x, N_y)$  being  $(5, 5), (7, 7), (8, 8), (9, 9)$  corresponding to  $N = 25, 49, 64, 81$  spins, where the Hamiltonian comprises the horizontal and vertical nearest neighbor interaction in two dimensions and a transverse magnetic field, 2D Euclidean RNN always emerge as the best ansatz, followed by 1D hyperbolic GRU, which almost always outperforms 1D Euclidean GRU, except for a single instance in the training result for  $(N_x, N_y) = (8, 8)$ . In this case, due to the artificial rearrangement or reshaping/folding of the 1D spin chain to mimic the 2D lattice, a hierarchy in the interaction structure, comprising the first and the  $N^{th}$  nearest neighbor interactions, is introduced when originally faraway spins (at site  $i$  and site  $i + N$ ) in the 1D chains become immediate vertical neighbors. The fact that the hyperbolic GRU NQS ansatz outperformed the Euclidean GRU NQS ansatz for this setting is our first clue of the role played by the hyperbolic geometry of the neural network in determining its performance when there is a hierarchical structure in the Hamiltonian.
- In the 1D Heisenberg  $J_1J_2$  setting with  $N = 50$  spins,  $J_1 = 1.0$  (fixed) and  $J_2 = 0.0, 0.2, 0.5, 0.8$ , hyperbolic GRU definitively outperforms Euclidean GRU three out of four times when the  $J_1J_2$  Hamiltonian exhibits a hierarchical interaction structure when  $J_2 \neq 0$  which takes into account the second nearest neighbor interactions in addition to the first nearest neighbor interactions. This is our second clue of the role played by the hyperbolic geometry of the neural network.
- In the 1D Heisenberg  $J_1J_2J_3$  setting with  $N = 30$  spins,  $J_1 = 1.0$  (fixed) and  $(J_2, J_3) = (0.0, 0.5), (0.2, 0.2), (0.2, 0.5), (0.5, 0.2)$ , hyperbolic GRU definitively outperforms Euclidean GRU four out of four times in the first set of experiments (where the networks have the same number of parameters), and three out of four times in the second set of VMC experiments (where the hyperbolic GRU network has around 10-20 percent fewer parameters than the Euclidean GRU network). In this setting, the  $J_1J_2J_3$  Hamiltonian exhibits even more pronounced hierarchical interaction structures comprising the first, second and third nearest neighbors. This is our third clue.

Given these findings, and the established results in natural language processing that hyperbolic RNNs almost always outperform their Euclidean versions when the training data exhibit hierarchical, tree-like structures [30], [35], [33], it is our hypothesis that hyperbolic RNN-based NQS will likely outperform Euclidean RNN-based NQS in all quantum spin systems in which there is a hierarchical structure in the interaction part of the Hamiltonian. More works are needed to confirm or refute this hypothesis. If true, this would be an exciting new direction opened up by the possibility of better performances delivered hyperbolic and potentially other non-Euclidean NQS in the problem of approximating the ground state energy of quantum many-body Hamiltonians using VMC - a problem that has been studied using exclusively conventional or Euclidean neural networks.

Several interesting generalizations exist given the results of this work. One immediate and specific direction involves the generalization of the one-dimensional hyperbolic GRU NQS in this work to two dimensions, and compare the performance of this 2D hyperbolic GRU against the 2D Euclidean GRU in the settings of 2D TFIM or 2D Heisenberg  $J_1J_2$  and  $J_1J_2J_3$  models. Other broader directions involve the exploration of a different type of hyperbolic RNNs, for example one that based on the Lorentz model of hyperbolic space instead of the Poincaré model [32], in various quantum many-body settings. Yet even more general directions involve the explorations of different types of non-Euclidean NQS beyond hyperbolic RNNs. These new types of non-Euclidean NQS could include, for example, the hyperbolic CNN networks [36] or the hyperbolic transformer neural network [32]. We leave these issues to future works.

## A Convergence curves

### A.1 1D TFIM

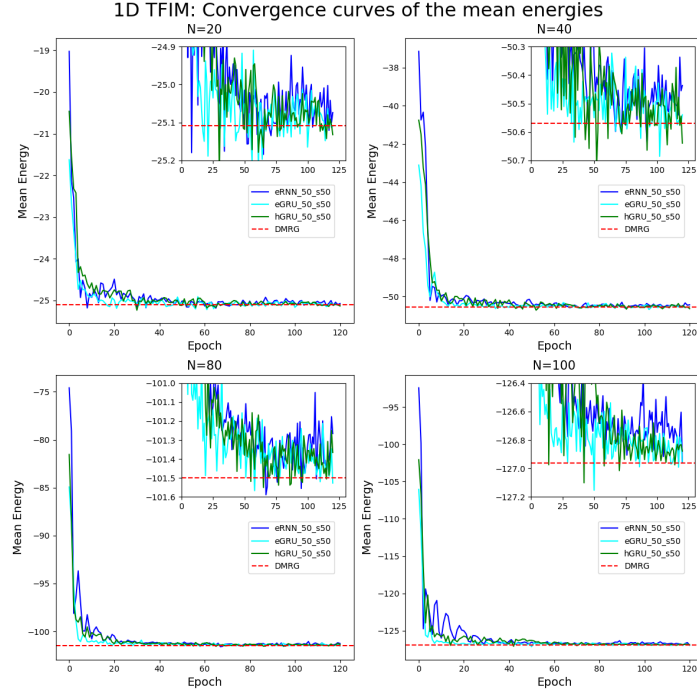


Figure 11: Convergence curves of the mean energy from the VMC experiments for 1D TFIM with various  $N$  (clockwise from top:  $N = 20, 40, 100, 80$  spins) with the three types of NQS ansatzes being eRNN-50-s50, eGRU-50-s50, hypGRU-50-s50. Each subfigure contains a zoomed-in plot showing a narrower range of energy values close to the exact DMRG value.

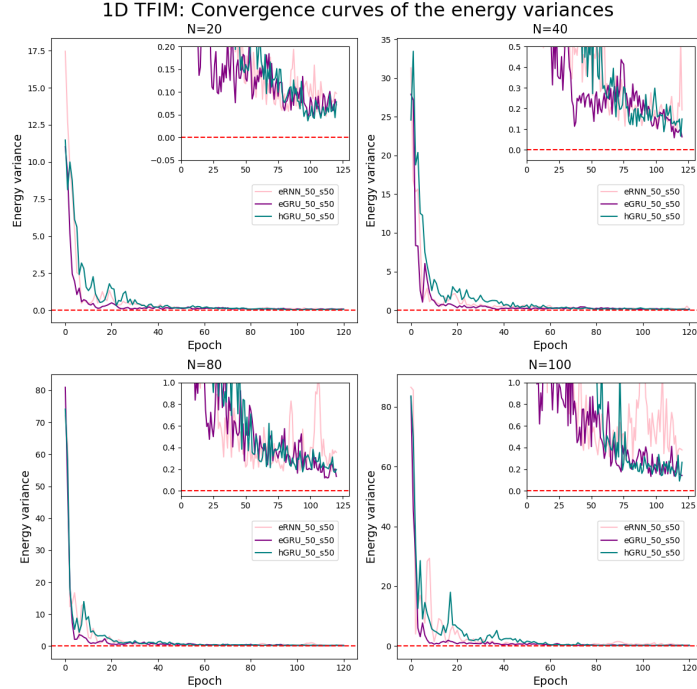


Figure 12: Convergence curves of the energy variances using eRNN-50-s50, eGRU-50-s50, hypGRU-50-s50 in VMC runs for 1D TFIM with various  $N$  (clockwise from top:  $N = 20, 40, 100, 80$  spins). The red dashed line corresponds to the line of zero variance. Each subfigure contains a zoomed-in plot showing a narrower range of variance values close to the zero line.

## A.2 2D TFIM

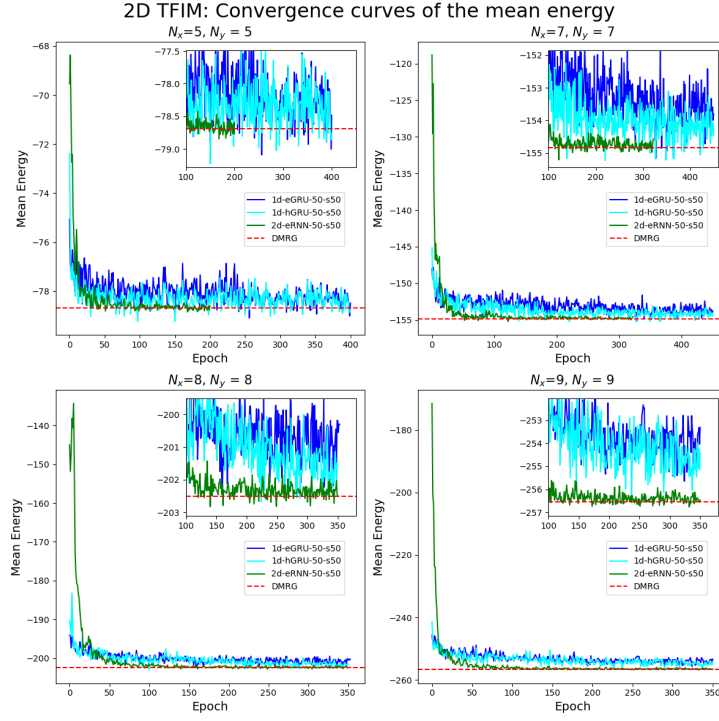


Figure 13: Convergence curves of the mean energy using 2D Euclidean RNN and 1D Euclidean/hyperbolic GRU ansatzes for the 2D TFIM with  $(N_x, N_y) = (5,5), (7,7), (9,9), (8,8)$  lattices (clockwise from top). Each subfigure contains a zoomed-in plot showing a narrower range of energy values close to the exact DMRG value.

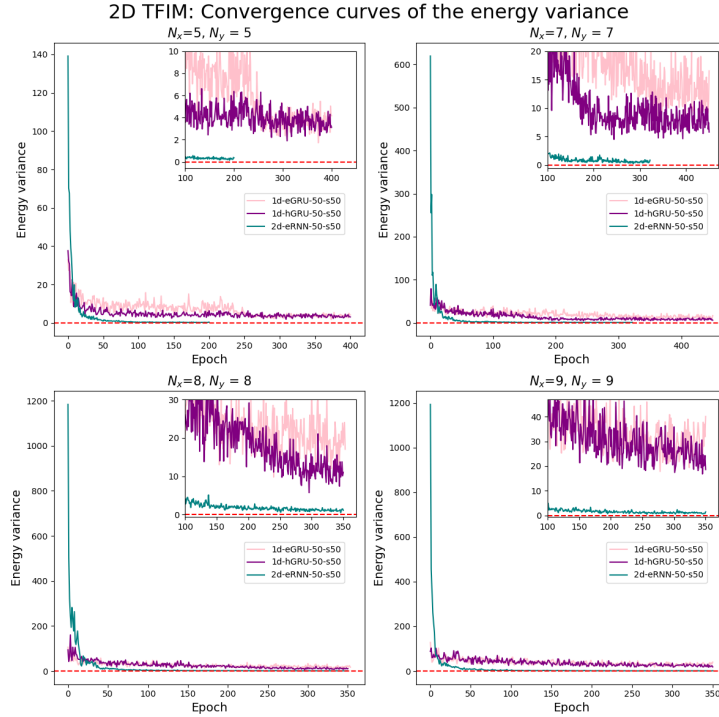


Figure 14: Convergence curves of the energy variances using 2D Euclidean RNN and 1D Euclidean/hyperbolic GRU ansatzes for the 2D TFIM with  $(N_x, N_y) = (5,5), (7,7), (9,9), (8,8)$  lattices (clockwise from top). The red dashed line corresponds to the line of zero variance. Each subfigure contains a zoomed-in plot showing a narrower range of variance values close to the zero line.

### A.3 1D Heisenberg $J_1 J_2$ model

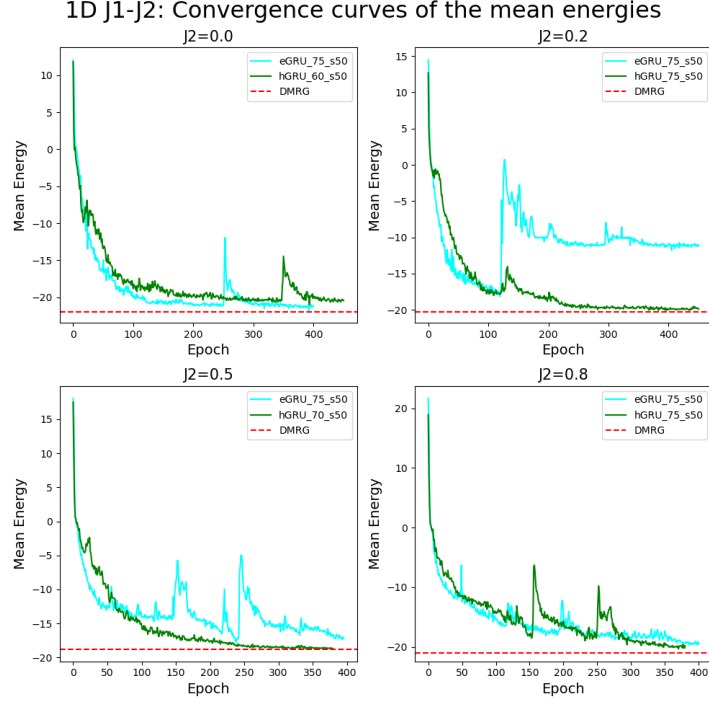


Figure 15: Convergence curves of the mean energy using Euclidean GRU and hyperbolic GRU from VMC runs of 1D Heisenberg  $J_1 J_2$  model with different  $J_2$  values - clockwise from top,  $J_2 = 0.0, 0.2, 0.8, 0.5$  - for  $N = 50$  spins.

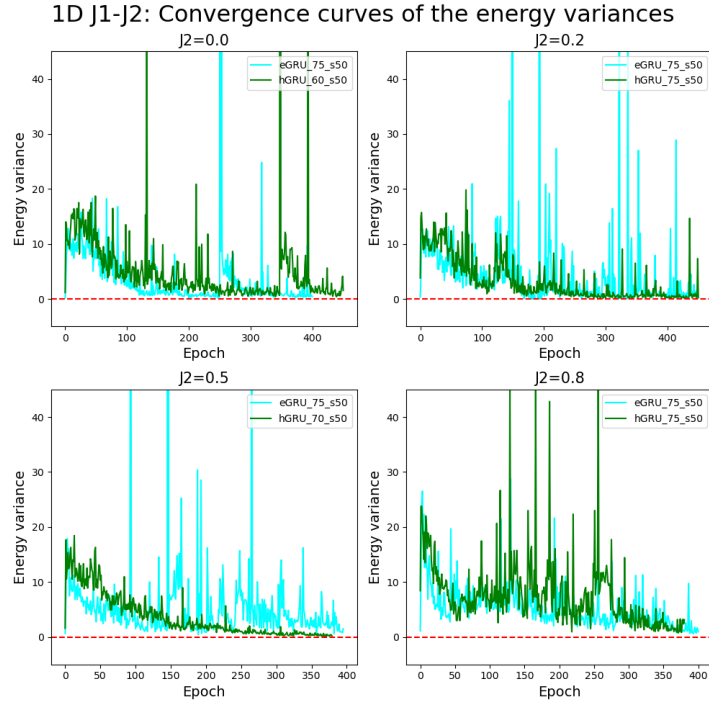


Figure 16: Convergence curves of the energy variances using Euclidean GRU and hyperbolic GRU from VMC runs of 1D Heisenberg  $J_1 J_2$  model with different  $J_2$  values - clockwise from top,  $J_2 = 0.0, 0.2, 0.8, 0.5$  - for  $N = 50$  spins. The red dashed line corresponds to the line of zero variance.

#### A.4 1D Heisenberg $J_1 J_2 J_3$ model

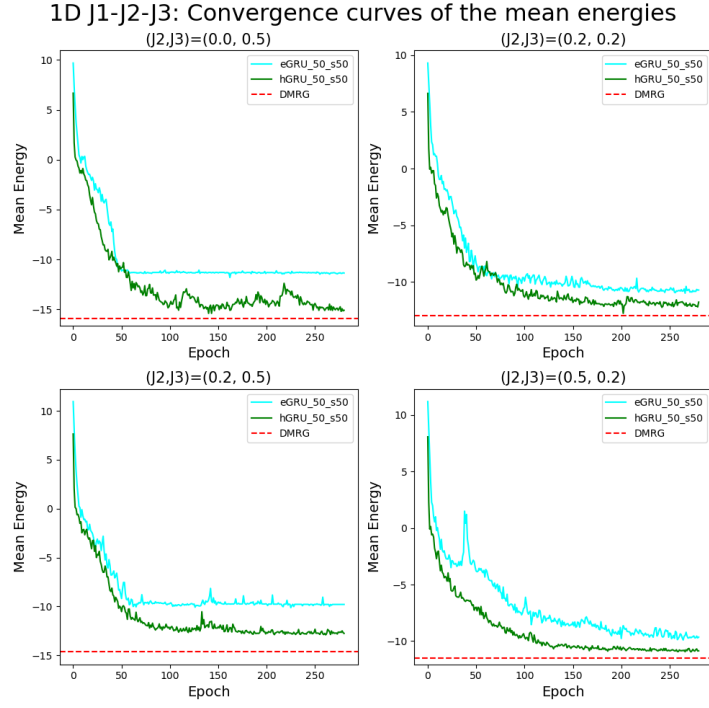


Figure 17: Convergence curves of the mean energy using Euclidean GRU and hyperbolic GRU from VMC runs of 1D Heisenberg  $J_1 J_2 J_3$  model with different  $(J_2, J_3)$  values - clockwise from top,  $(J_2, J_3) = (0.0, 0.5)$ ,  $(0.2, 0.2)$ ,  $(0.5, 0.2)$ ,  $(0.2, 0.5)$  - for  $N = 30$  spins.

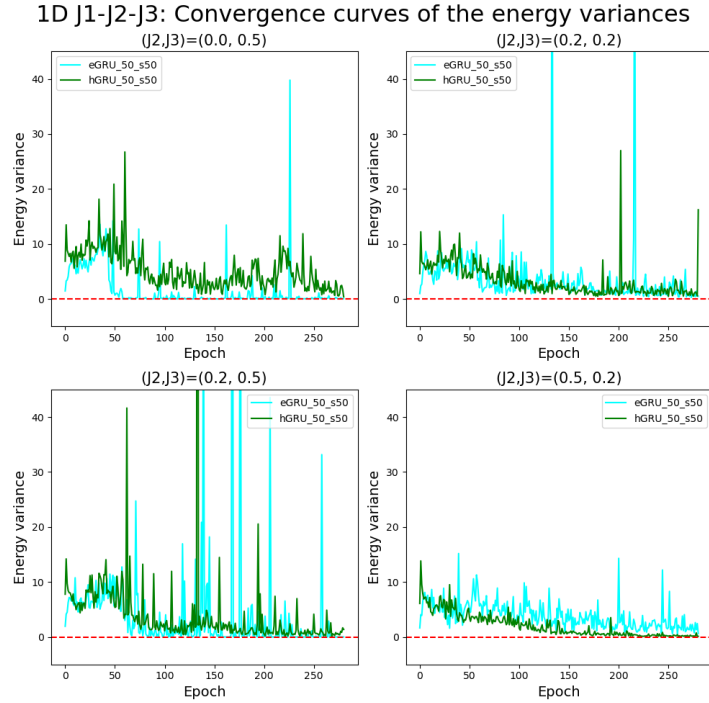


Figure 18: Convergence curves of the energy variances using Euclidean GRU and hyperbolic GRU from VMC runs of 1D  $J_1 J_2 J_3$  Heisenberg model with different  $(J_2, J_3)$  values - clockwise from top,  $(J_2, J_3) = (0.0, 0.5)$ ,  $(0.2, 0.2)$ ,  $(0.5, 0.2)$ ,  $(0.2, 0.5)$ - for  $N = 30$  spins. The red dashed line corresponds to the line of zero variance.

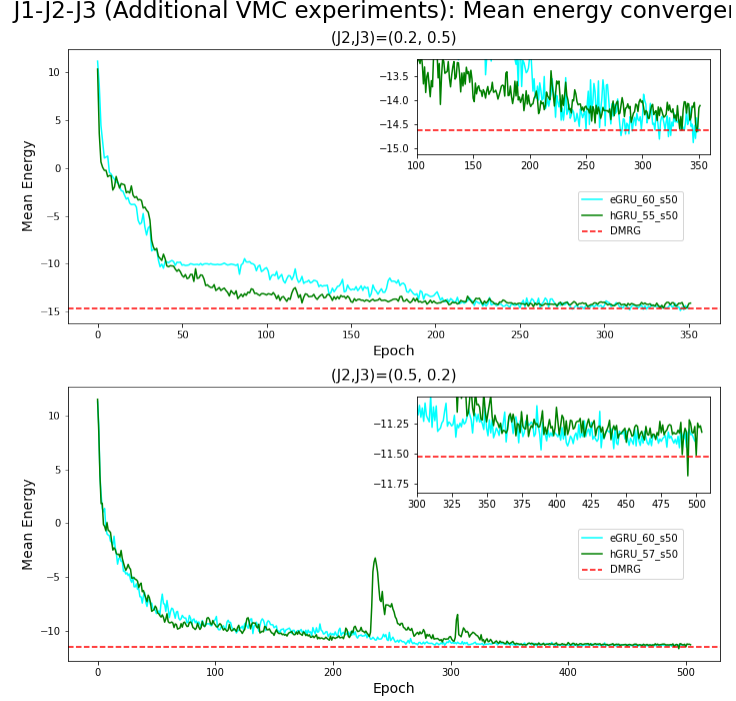


Figure 19: Convergence curves of the mean energy using Euclidean GRU and hyperbolic GRU from VMC runs of 1D Heisenberg  $J_1 J_2 J_3$  model with different  $(J_2, J_3)$  values - from top to bottom,  $(J_2, J_3) = (0.2, 0.5), (0.5, 0.2)$  - for  $N = 30$  spins. Each subfigure contains a zoomed-in plot showing a narrower range of energy values close to the exact energy line.

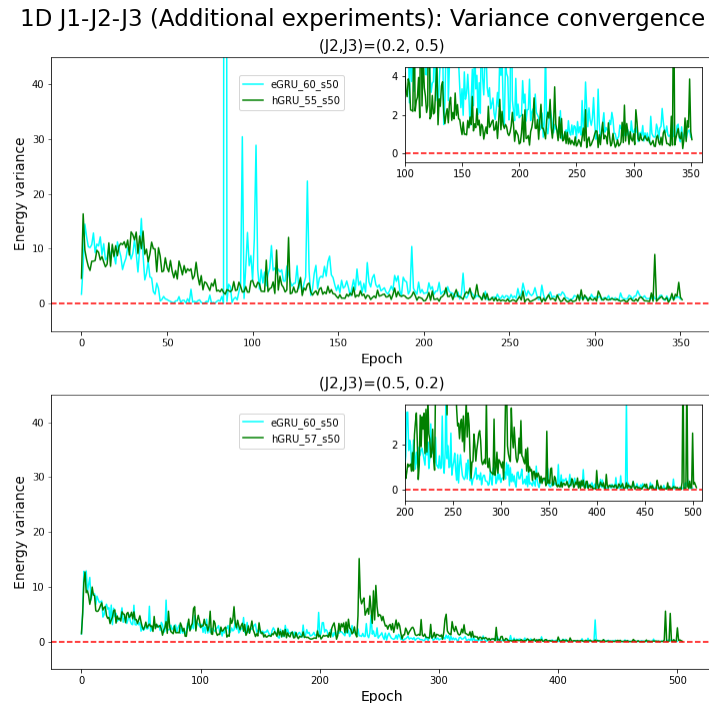


Figure 20: Convergence curves of the energy variances using Euclidean GRU and hyperbolic GRU from VMC runs of 1D  $J_1 J_2 J_3$  Heisenberg model with different  $(J_2, J_3)$  values - from top to bottom,  $(J_2, J_3) = (0.2, 0.5), (0.5, 0.2)$  - for  $N = 30$  spins. The red dashed line corresponds to the line of zero variance. Each subfigure contains a zoomed-in plot showing a narrower range of variance values close to the zero line.

## References

- [1] G. Carleo and M. Troyer, Solving the Quantum Many-Body Problem with Artificial Neural Networks, *Science* 355, 602 (2017), arXiv:1606.02318 [cond-mat.dis-nn]
- [2] Z. Cai and J. Liu, Approximating quantum many-body wave-functions using artificial neural networks, *Phys. Rev. B* 97, 035116 (2018), arXiv:1704.05148 [cond-mat.str-el]
- [3] H. Saito and M. Kato, Machine learning technique to find quantum many-body ground states of bosons on a lattice, *J. Phys. Soc. Jpn.* 87, 014001 (2018), arXiv:1709.05468 [cond-mat.dis-nn]
- [4] L. Huang and L. Wang, Accelerate Monte Carlo Simulations with Restricted Boltzmann Machines, arXiv:1610.02746v2.
- [5] O. Sharir, Y. Levine, N. Wies, G. Carleo, and A. Shashua, Deep autoregressive models for the efficient variational simulation of quantum many-body systems, arXiv:1902.0405
- [6] X. Liang, Wen-Yuan Liu, Pei-Ze Lin, Guang-Can Guo, Yong-Sheng Zhang, and Lixin He, Solving frustrated quantum many-particle models with convolutional neural networks, arXiv: 1807.09422v2
- [7] K. Choo, T. Neupert, and G. Carleo, Study of the Two-Dimensional Frustrated J1-J2 Model with Neural Network Quantum States, arXiv:1903.06713v1
- [8] C. Roth, A. Szabó, and A. H. MacDonald, High-accuracy variational Monte Carlo for frustrated magnets with deep neural networks, *Phys. Rev. B* 108, 054410 (2023), arXiv:2211.07749v2 [cond-mat.str-el]
- [9] M. Hibat-Allah, M. Ganahl, L. E. Hayward, R. G. Melko, and J. Carrasquill, Recurrent neural network wave functions, *Physical Review Research* 2, 023358 (2020).
- [10] M. Hibat-Allah, R. G. Melko, J. Carrasquilla, Supplementing Recurrent Neural Network Wave Functions with Symmetry and Annealing to Improve Accuracy, *Machine Learning and the Physical Sciences, NeurIPS 2021*, arXiv:2207.14314v2 [cond-mat.dis-nn]
- [11] M. Hibat-Allah, E. Merali, G. Torlai, R. G. Melko and J. Carrasquilla, Recurrent neural network wave functions for Rydberg atom arrays on kagome lattice, arXiv:2405.20384v1 [cond-mat.quant-gas]
- [12] M. S. Moss, R. Wiersema, M. Hibat-Allah, J. Carrasquilla and R. G. Melko, Leveraging recurrence in neural network wavefunctions for large-scale simulations of Heisenberg antiferromagnets: the square lattice, arXiv:2502.17144 [cond-mat.str-el]
- [13] T. Vieijra, C. Casert, J. Nys, W. De Neve, J. Haegeman, J. Ryckebusch, and F. Verstraete, Restricted Boltzmann Machines for Quantum States with Nonabelian or Anyonic Symmetries, arXiv:1905.06034.
- [14] E. Rinaldi, X. Han, M. Hassan, Y. Feng, F. Nori, M. McGuigan, and M. Hanada, Matrix-Model Simulations Using Quantum Computing, Deep Learning, and Lattice Monte Carlo, *PRX Quantum* 3, 010324 (2022).
- [15] L. L. Viteritti, R. Rende and F. Becca, Transformer variational wave functions for frustrated quantum spin systems, *Phys. Rev. Lett.* 130, 236401 (2023), arXiv:2211.05504 [cond-mat.dis-nn]
- [16] L. L. Viteritti, R. Rende, A. Parola, S. Goldt, and F. Becca, Transformer wave function for two dimensional frustrated magnets: emergence of a spin-liquid phase in the shastry-sutherland model (2024), arXiv:2311.16889 [cond-mat.str-el].
- [17] K. Sprague and S. Czischek, Variational Monte Carlo with Large Patched Transformers, *Commun Phys* 7, 90 (2024), arXiv:2306.03921 [quant-ph]
- [18] H. Lange, G. Bornet, G. Emperaiger, C. Chen, T. Lahaye, S. Kienle, A. Browaeys, A. Bohrdt, Transformer neural networks and quantum simulators: a hybrid approach for simulating strongly correlated systems, *Quantum* 9, 1675 (2025), arXiv:2406.00091 [cond-mat.dis-nn]
- [19] R. Rende and L. L. Viteritti, Are queries and keys always relevant? a case study on transformer wave functions, *Machine Learning: Science and Technology* 6, 010501 (2025).
- [20] H. Saito, Solving the Bose–Hubbard Model with Machine Learning, *J. Phys. Soc. Jpn.* 86 (2017) 093001.
- [21] H. Saito and M. Kato, Machine Learning Technique to Find Quantum Many-Body Ground States of Bosons on a Lattice, *J. Phys. Soc. Jpn.* 87 (2018) 014001.

[22] Y. Nomura, A. S. Darmawan, Y. Yamaji, and M. Imada, Restricted-Boltzmann-Machine Learning for Solving Strongly Correlated Quantum Systems, *Phys. Rev. B* 96 (2017) 205152, arXiv:1709.06475 [cond-mat.str-el]

[23] D. Luo and B. K. Clark, Backflow Transformations via Neural Networks for Quantum Many-Body Wave-Functions, *Phys. Rev. Lett.* 122 (2019) 226401, arXiv:1807.10770 [cond-mat.dis-nn]

[24] J. Han, L. Zhang, and W. E, Solving Many-Electron Schrödinger Equation Using Deep Neural Networks, *Journal of Computational Physics*, 399, 108929 (2019), arXiv:1807.07014 [physics.comp-ph]

[25] K. Choo, A. Mezzacapo, and G. Carleo, Fermionic neural-network states for ab-initio electronic structure, arXiv:1909.12852v1 [physics.comp-ph]

[26] R. Rende, L. L. Viteritti, F. Becca, A. Scardicchio, A. Laio and G. Carleo, Foundation Neural-Network Quantum States, arXiv:2502.09488v1 [quant-ph]

[27] Y. Nomura, Machine Learning Quantum States – Extensions to Fermion-Boson Coupled Systems and Excited-State Calculations, *J. Phys. Soc. Jpn.* 89, 054706 (2020), arXiv:2001.02106v3 [cond-mat.str-el]

[28] H. Lange, A. Van de Walle, A. Abedinnia and A. Bohrdt, From Architectures to Applications: A Review of Neural Quantum States, *Quantum Sci. Technol.* 9 040501, arXiv:2402.09402 [cond-mat.dis-nn]

[29] F. Becca and S. Sorella, Quantum Monte Carlo approaches for correlated systems, Cambridge University Press 2017, DOI: 10.1017/9781316417041

[30] O.-E. Ganea, G. Bécigneul, and T. Hofmann, Hyperbolic Neural Networks, *Advances in Neural Information Processing Systems* 31, pages 5345–5355. Curran Associates, Inc. arXiv: 1805.09112 [cs.LG]

[31] M. Nickel and D. Kiela, Learning Continuous Hierarchies, in the Lorentz Model of Hyperbolic Geometry, *ICML* 2018, arXiv:1806.03417 [cs.AI]

[32] W. Chen, X. Han, Y. Lin, H. Zhao, Z. Liu, P. Li, M. Sun, J. Zhou, Fully Hyperbolic Neural Networks, in *ACL 2022 Main Conference*, arXiv:2105.14686 [cs.CL].

[33] W. Peng, T. Varanka, A. Mostafa, H. Shi, G. Zhao, Hyperbolic Deep Neural Networks: A Survey, arXiv:2101.04562 [cs.LG, cs.CV]

[34] C. Gulcehre, M. Denil, M. Malinowski, A. Razavi, R. Pascanu, et. al., Hyperbolic Attention Networks, arXiv:1805.09786v1 [cs.NE]

[35] F. Lopez and M. Strube, A Fully Hyperbolic Neural Model for Hierarchical Multi-Class Classification, *Findings of EMNLP2020*, arXiv:2010.02053 [cs.CL].

[36] R. Shimizu, Y. Mukuta and T. Harada, Hyperbolic Neural Networks++, *The Ninth International Conference on Learning Representations (ICLR 2021)*, arXiv:2006.08210 [cs.LG]

[37] E. Mathieu, C. Le Lan, C. J. Maddison, R. Tomioka, and Y. W. Teh, Continuous Hierarchical Representations with Poincaré Variational Auto-Encoders, arXiv:1901.06033.

[38] G. Bachmann, G. Bécigneul, O.-E. Ganea, Constant Curvature Graph Convolutional Networks, arXiv:1911.05076v3.

[39] H. W. J. Blöte and Y. Deng, Cluster Monte Carlo simulation of the transverse Ising model, *Phys. Rev. E* 66, 066110 (2002)

[40] N. Bodendorfer, O. Oktay, V. Gautam, M. Hanada, and Enrico Rinaldi, Variational Monte Carlo with Neural Network Quantum States for Yang-Mills Matrix Model, arXiv:2409.00398v1

[41] S. Bonnabel, Stochastic gradient descent on riemannian manifolds, *IEEE Transactions on Automatic Control*, 58(9):2217–2229, Sept 2013.

[42] O.-E. Ganea, G. Bécigneul, and T. Hofmann. Hyperbolic entailment cones for learning hierarchical embeddings. In *Proceedings of the thirty-fifth international conference on machine learning (ICML)*, 2018

[43] G. Bécigneul and O.-E Ganea, Riemannian Adaptive Optimization Methods, *International Conference on Learning Representations (ICLR)* (2019), arXiv:1810.00760 [cs.LG]

[44] S. R. White and I. Affleck, Dimerization and incommensurate spiral spin correlations in the zigzag spin chain: Analogies to the Kondo lattice, *Phys. Rev. B* 54, 9862 (1996).

- [45] S. Eggert, Numerical evidence for multiplicative logarithmic corrections from marginal operators, *Phys. Rev. B* 54, R9612(R) (1996).
- [46] F. Becca, L. Capriotti, A. Parola, and S. Sorella, Variational Wave Functions for Frustrated Magnetic Models, in *Introduction to Frustrated Magnetism: Materials, Experiments, Theory*, edited by C. Lacroix, P. Mendels, and F. Mila (Springer, Berlin, Heidelberg, 2011), pp. 379–406.
- [47] W. Marshall, Antiferromagnetism, *Proc. R. Soc. A* 232, 48 (1955).
- [48] R. Zinke, J. Richter, and S.-L. Drechsler, Spiral correlations in frustrated one-dimensional spin-1/2 Heisenberg J1-J2-J3 ferromagnets, *J. Phys.: Condens. Matter* 22, 446002 (2010), arXiv:1008.0317 [cond-mat.str-el]